

# 1 Seismo-acoustic and GNSS observations of a record-breaking Black 2 Sea storm: repurposing geophysical sensors for environmental 3 monitoring 4

5 Laura Petrescu<sup>1,2,\*</sup>, Bogdan Antonescu<sup>1,2</sup>, Sorin Nistor<sup>3</sup>, Iustin Floroiu<sup>4,5</sup>, Dragoş Ene<sup>1</sup>, Daniela  
6 Ghica<sup>1</sup>, Constantin Ionescu<sup>1</sup>, Andrei Anghel<sup>4</sup>, Mihai Datcu<sup>4</sup>  
7

- 8 1. National Institute for Earth Physics, Magurele, Romania
- 9 2. University of Bucharest, Faculty of Physics, Magurele, Romania
- 10 3. University of Oradea, Faculty of Construction, Cadaster and Architecture, Oradea,  
11 Romania
- 12 4. Politehnica University of Bucharest, Faculty of Electronics, Telecommunications and  
13 Information Technology, Bucharest, Romania
- 14 5. Politehnica University of Bucharest, Doctoral School of Electronics,  
15 Telecommunications & Information Technology, Bucharest, Romania

16  
17 \* laura.petrescu@infp.ro  
18

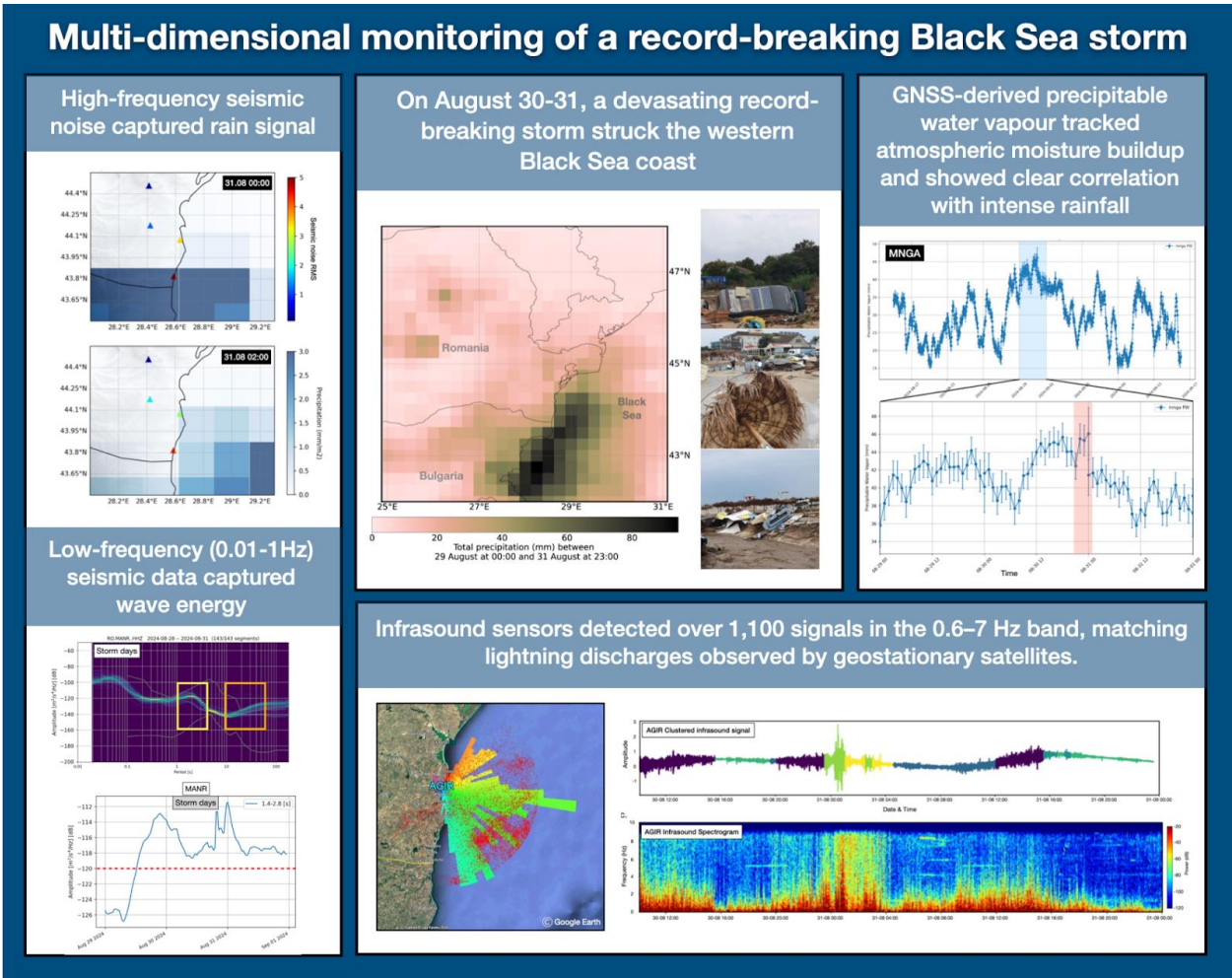
## 19 Abstract 20

21 In August 2024, a devastating storm struck Romania’s Black Sea coast, setting new precipitation  
22 records and marking an unusual change relative to historical climate observations. To investigate  
23 this extraordinary event, we integrated non-conventional sensors (seismic, GNSS, infrasound, and  
24 satellite data) with ERA5 meteorological reanalysis to monitor storm dynamics. High-frequency  
25 (>30 Hz) seismic signals captured precipitation, while microseismic bands (0.1-1Hz) reflected  
26 wave-induced ground motion. Analysis of infrasound data via unsupervised learning delineated  
27 periods of acoustic quiescence from storm-related activity. The temporal evolution of these  
28 infrasound states coincided with distinct patterns in seismic ground motion, suggesting a shared  
29 origin in the storm's atmospheric dynamics. The infrasound array also detected over 1,100 signals  
30 in the 0.6-7 Hz band, matching lightning discharges observed by geostationary satellites. GNSS  
31 data recorded a buildup of precipitable water vapor that peaked concurrently with intense rainfall,  
32 following a multi-day increase that preceded the main storm phase. This study highlights the value  
33 of integrating diverse, non-traditional datasets to enhance the resolution and depth of storm  
34 analysis. Their combined use offers a more holistic understanding of storm evolution and supports  
35 future research on the potential role of multi-sensor observations in improving early-warning  
36 systems in vulnerable coastal regions.

37

38 **Graphical abstract**

39



40

41

42

43

44

45

46

47

## 48 **1. Introduction**

49 Climate change has become a critical global issue, with far-reaching effects on weather patterns  
50 and the frequency and intensity of extreme events (Stott, 2016). These changes are not only  
51 contributing to more severe weather events but also altering the timing, location, and duration of  
52 storms, making them harder to predict and manage (Bengtsson et al., 2006). Understanding how  
53 to effectively monitor and predict the behavior of storms, particularly extreme ones, is crucial for  
54 improving forecasting models, enhancing early warning systems, and mitigating their impacts on  
55 both natural and human systems.

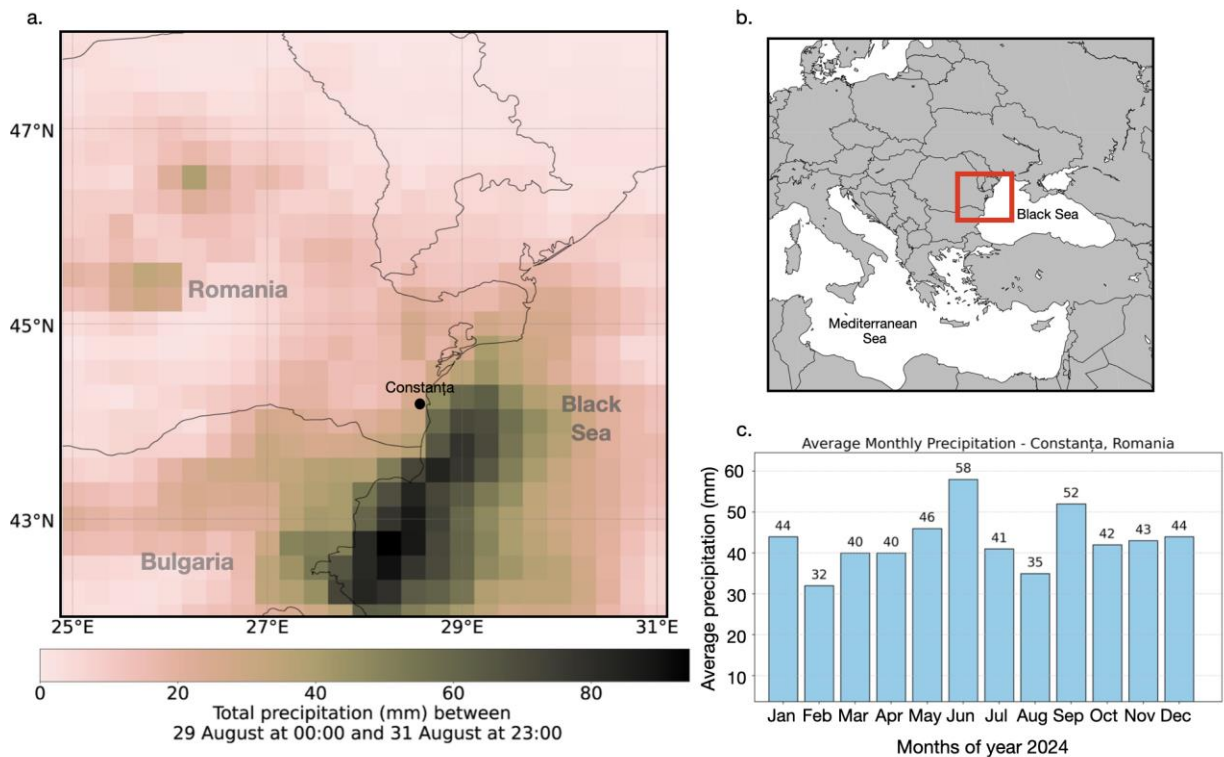
56 Traditional meteorological monitoring relies heavily on ground-based stations, weather radars, and  
57 satellite observations to track and predict storm behavior (Kober and Tafferner, 2009). These  
58 systems have been the backbone of weather forecasting for decades, providing valuable data on  
59 temperature, pressure, wind speed, and precipitation. However, while these methods are effective,  
60 they often have limitations in terms of spatial coverage (e.g. Sokol et al., 2021), particularly in  
61 remote or hard-to-reach areas. Additionally, they may struggle to capture certain atmospheric  
62 phenomena in real-time. As a result, non-conventional monitoring methods are increasingly being  
63 integrated into storm tracking efforts to complement existing meteorological approaches (e.g. Bosity  
64 et al., 2012; Burtin et al., 2016; Diaz et al., 2023; Coviello et al., 2024).

65 In this context, our study focuses on the integration of alternative environmental datasets, including  
66 GNSS stations, infrasound sensors, and seismic data, to track the dynamics of an extreme storm  
67 event, as part of a national climate change resilience strategy, implemented through the DTE  
68 Climate project (<https://dteclimate.upb.ro/>). GNSS data provide valuable information on  
69 atmospheric water vapor, helping to track moisture changes that influence storm formation and  
70 intensity (Bosity et al, 2012; Marut et al., 2022). Infrasound sensors detect low-frequency acoustic  
71 waves generated by storm activity, such as lightning or large-scale weather system movements  
72 like microbaroms (e.g. Landès et al., 2012). Seismic data, though traditionally used for earthquake  
73 monitoring, can also record vibrations caused by storm-induced pressure changes, making it useful  
74 for detecting rainstorms, floods, or tropical cyclones (e.g. Retailleau and Gualtieri, 2021). Through  
75 the integration of these diverse sensor networks, our work highlights their synergy in improving  
76 storm detection, monitoring capabilities, and, potentially, early warning systems, contributing to  
77 more robust climate resilience strategies.

## 78 **2. Study area and storm overview**

79  
80 The Black Sea region (Figure 1) is characterized by a unique combination of geographic and  
81 meteorological features that significantly influence its climate and weather patterns. Nestled  
82 between Europe and Asia, the Black Sea is bordered by six countries with diverse landscapes, from  
83 mountainous areas to flat plains. This geography, combined with the Black Sea's relatively shallow  
84 waters compared to oceanic environments and its connection to the Mediterranean through the  
85 Bosphorus Strait, creates an environment where rapid changes in weather are common.  
86 Understanding the dynamics of these extreme weather events is crucial, as they can have a  
87 profound impact on the environment, economy, and daily life in the region. Monitoring such events  
88 is key to improving our ability to predict their occurrence and intensity. By studying the complex  
89 atmospheric processes that govern these storms, we can enhance predictive models and refine early

90 warning systems, ultimately helping to mitigate the risks and protect the communities and  
91 ecosystems most vulnerable to these extreme weather phenomena.



92  
93 *Figure 1. a. Total precipitation accumulated (in mm, shaded according to the scale) between 29*  
94 *August 00 UTC and 31 August 23:00 UTC extracted from ERA5 data. b. Map of Europe with red*  
95 *square marking the study region; c. Average monthly precipitation rates in Constanța, Romania.*

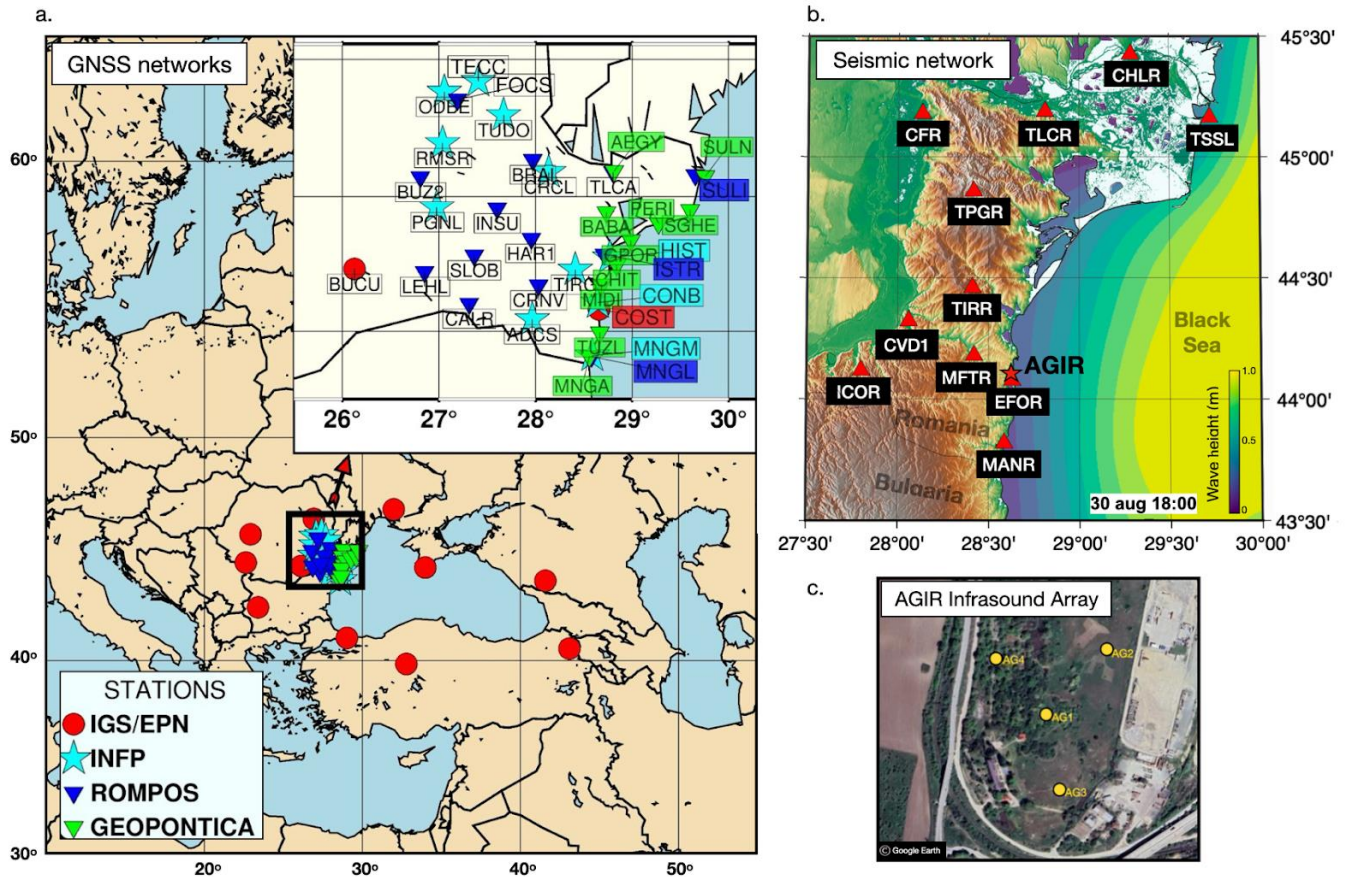
96 In August 2024, Romania experienced severe flooding, largely driven by a storm that brought  
97 unusual precipitation patterns to the Black Sea coastal region. Exceptional precipitation totals were  
98 recorded over south-eastern Romania in particular in Mangalia (234.7 mm), Agigea (145 mm),  
99 and Tuzla (118 mm), leading to significant flooding in coastal towns (Figure 1). Over 800  
100 emergency calls prompted large-scale intervention by ISU Dobrogea, focusing on evacuations,  
101 debris clearance, and infrastructure restoration (Antonescu et al. 2024). According to the National  
102 Meteorological Agency official records ([https://www.meteoromania.ro/clim/caracterizare-](https://www.meteoromania.ro/clim/caracterizare-lunara/cc_2024_08.html)  
103 [lunara/cc\\_2024\\_08.html](https://www.meteoromania.ro/clim/caracterizare-lunara/cc_2024_08.html)), one of the coastal stations at Mangalia, recorded a total of 343.6 mm of  
104 precipitation in August 2024, breaking the previous record of 159.1 mm from 1947, and  
105 significantly surpassing the average monthly precipitation values for this area (Figure 1c). A  
106 remarkable 234.7 mm of this total fell in a single day on August 31, 2024, highlighting the event's  
107 exceptional intensity.

108 An analysis by ClimaMeter ([www.climameter.org](http://www.climameter.org), Faranda et al. 2024, Antonescu et al. 2024)  
109 immediately after the storm, showed that low pressure systems similar to the one that caused the  
110 floods typically produce 15% less rainfall in eastern Romania compared to historical trends.  
111 However, this particular storm led to a significant local increase in precipitation, particularly in  
112 Constanța, where daily rainfall reached up to 5 mm day<sup>-1</sup>, or up to 10% more than usual.

113 ClimaMeter’s analysis compares events of this type to historical analogues over the past several  
114 decades, providing context for how unusual this storm was. According to Antonescu et al. (2024),  
115 the local precipitation anomaly in this event is mostly linked to human-induced climate change,  
116 with natural climate variability playing a modest role. Studying this unusual storm and its  
117 atmospheric characteristics demonstrates the value of using all available observational  
118 infrastructure, including geophysical sensors, to monitor extreme precipitation events, gain  
119 insights into atmospheric processes, and support preparedness and resilience in the context of  
120 ongoing climate variability.

### 121 **3. Data and Methods**

122 The analysis of the storm event integrates a variety of data sources and methodologies to provide  
123 a comprehensive understanding of its dynamics. Seismic data, infrasound measurements, GNSS  
124 water vapor data, and ERA5 reanalysis data are all utilized to capture different aspects of the  
125 storm’s behavior (Figure 2). Seismic data offers insights into ground vibrations and atmospheric  
126 disturbances, while infrasound monitoring detects low-frequency acoustic signals generated by  
127 lightning and other meteorological phenomena. GNSS water vapor data provides valuable  
128 information on atmospheric moisture. Additionally, ERA5 reanalysis data (Hersbach et al. 2020),  
129 which provides detailed atmospheric and wave dynamics data, helps contextualize the storm's  
130 impact within broader weather patterns. Together, these diverse data sources enable a multifaceted  
131 approach to studying the storm and its effects.



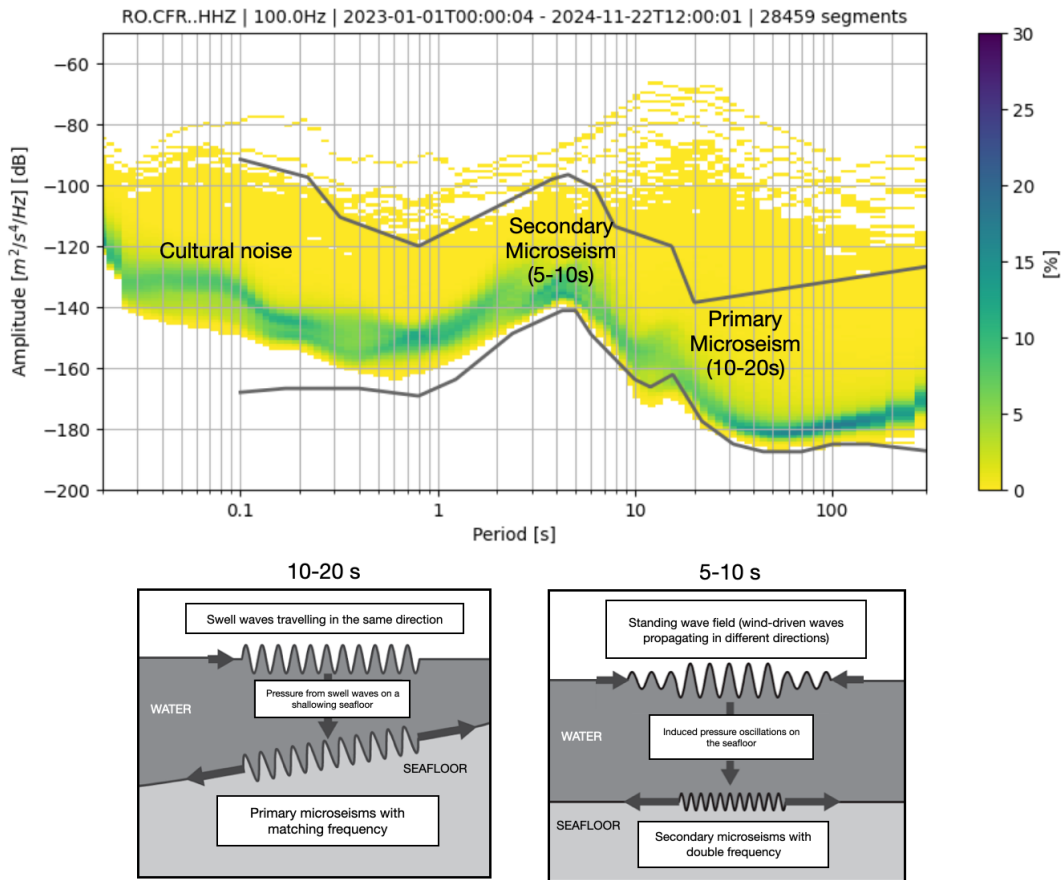
132  
 133 *Figure 2. a. Map of Europe and the Black Sea coast showing GNSS stations and their belonging networks*  
 134 *used for analysis in this study. b. Map of the Romanian sea coast showing seismic stations (red triangles)*  
 135 *and the location of the AGIR infrasound array (star). Coloured contours represent total wave height at*  
 136 *18:00 UTC on the 30th of August 2024 from ERA5 reanalysis data. c. The layout of the AGIR infrasound*  
 137 *array.*

138  
 139 **3.1 Seismic Data**

140 Seismic data represents vibrations of the Earth's surface, commonly referred to as seismic noise.  
 141 These low-amplitude movements are recorded across the Earth's surface and are traditionally used  
 142 to study the Earth's internal structure and detect earthquakes. Recently, it has increasingly found  
 143 applications in meteorology and hydrology, particularly for monitoring weather events (e.g. Dias  
 144 et al. 2023; Hua et al., 2023), destructive flood episodes (Burtin et al., 2016), ocean storms, and  
 145 tropical cyclones (Gualtieri et al., 2018). Seismic noise can reveal the impact of atmospheric and  
 146 oceanic conditions, providing valuable insights into weather events and climate changes (e.g.  
 147 Bromirski et al., 2002; Aster et al, 2008; 2023). In particular, seismic data helps track variations  
 148 in the Earth's surface caused by factors such as ocean waves, wind, and precipitation, offering a  
 149 unique perspective on these phenomena (e.g. Grevemeyer et al., 2000; Borzi et al., 2022).

150 When the seismic noise is analyzed in the frequency domain, two clear peaks emerge in the  
 151 spectrum (Figure 3), reflecting distinct types of ocean wave interactions (Koper et al., 2015;

152 Arduin et al., 2019; Tanimoto et al., 2023). The primary peak, observed in the range of 10-20  
 153 seconds (0.05-1 Hz), is generated by the impact of "swell" waves traveling in the same direction,  
 154 inducing pressure variations in the Earth's crust that match the period of the waves. The secondary  
 155 peak, in the range of 5-10 seconds (0.1-0.5 Hz), is produced by wind-driven waves, which  
 156 propagate in different directions and generate pressure oscillations on the ocean floor (Ebeling et  
 157 al., 2012). These seismic signals directly link ocean conditions with seismic activity (Li et al.,  
 158 2020), providing insights into large-scale weather phenomena like ocean storms.



159  
 160 *Figure 3. Probabilistic Power Spectral Density (PPSD) of seismic noise for station CFR, over two years,*  
 161 *showing key sources of primary and secondary microseisms. Below, sketches illustrate the generation*  
 162 *mechanisms: primary microseisms are caused by unidirectional swell waves inducing pressure fluctuations*  
 163 *on a shoaling seafloor, while secondary microseisms result from nonlinear interactions of wind-driven*  
 164 *waves over deeper water (modified after Ebeling, 2012).*

165 Higher frequencies above 30 Hz are associated with the effects of precipitation and wind, as seen  
 166 in studies like Rindraharisaona et al. (2022) or Diaz et al. (2023). These higher-frequency seismic  
 167 signals help track more localized weather events, such as storms and heavy rainfall. Seismic data,  
 168 when integrated with other meteorological tools, enhances the ability to monitor and predict  
 169 weather events.

170 To analyse seismic data, the raw traces are first corrected for instrument response and converted  
171 to units of velocity. These are then filtered with bandpass butterworth filters adapted to capture the  
172 target signal: low pass filtering (<1 Hz) for wave-seafloor coupled interactions and high pass  
173 filtering (>30 Hz) to identify possible signatures of precipitation, essentially induced pressure  
174 fluctuations in the ground converted to weak seismic vibrations due to rain drops. Spectrograms  
175 of these filtered seismic traces were computed using short-time Fourier transforms implemented  
176 in the `scipy.signal` package, with the default 256-sample window length used for each segment,-to  
177 visualise signatures of the hydro-meteorological phenomena in the frequency content of ground  
178 vibrations.

179 Potential environmental signals in the seismic data were also investigated using power spectral  
180 density (PSD) analysis. To account for variations over time, a Probabilistic Power Spectral Density  
181 (PPSD) method was applied. The continuous waveform was divided into 1-hour time windows  
182 with 50% overlap, and a PSD was computed for each window after instrument-response correction  
183 and basic preprocessing. These estimates were combined into a probability distribution, providing  
184 a statistical overview of typical and transient noise levels across frequencies. The PPSD was  
185 produced using ObsPy (Beyreuther et al., 2010), which handles data gaps and ensures reliable  
186 normalization.

187 Temporal variations in PSD amplitudes are also analyzed to track changes in seismic noise at  
188 specific frequencies. By extracting PSD values at selected frequencies that are expected to capture  
189 primary and secondary microseisms, time series of noise levels are generated. These temporal  
190 PSDs allow for the identification of trends and correlations with environmental factors, such as  
191 ocean wave activity or weather conditions.

## 192 **3.2 Acoustic Data**

193 Infrasound waves are low-frequency acoustic waves that are inaudible to the human ear, typically  
194 below 20 Hz. These waves are generated by a variety of natural and anthropogenic sources,  
195 including meteorological events, volcanic eruptions, earthquakes, and human activities such as  
196 explosions and industrial processes (Campus and Christie, 2009; Bondár et al., 2022). In particular,  
197 infrasound is often associated with phenomena like thunderstorms, ocean waves, and large-scale  
198 atmospheric events, which generate pressure fluctuations that propagate through the atmosphere  
199 (e.g. Stopa et al., 2012; Landès et al., 2012; Listowski et al., 2022). These waves provide valuable  
200 information about the dynamics of weather systems (e.g. Hupe et al., 2019), making them an  
201 essential tool for monitoring and understanding environmental processes (e.g. Brachet et al., 2009;  
202 Hupe et al., 2022). Infrasound associated with thunderstorms, primarily generated by acoustic  
203 waves from thunder, has been studied previously and shown to be detectable at distances ranging  
204 from tens to hundreds of kilometers (e.g., Assink et al., 2008; Sindelarova et al., 2015; Šindelářová  
205 et al., 2021). Nevertheless, infrasound arrays detect signals from multiple storm-related sources,  
206 not just thunder (e.g., Waxler et al., 2024). In the present study, we build on this understanding by  
207 integrating these signals with seismic, satellite, meteorological, and water vapor observations to  
208 investigate what these complementary datasets reveal about storm evolution in a coastal  
209 environment.

210 For the monitoring of infrasound signals, we use data from an infrasound array system located at  
211 Eforie Nord-Agigea, Romania (AGIR, Figure 2). This array consists of multiple sensors, including

212 SIS-1 infrasonic sensors (Seismowave), equipped with global positioning systems (GPS) and noise  
213 reduction technology.

214 To analyze the seismo-acoustic characteristics of the August 30-31 Black Sea storm, we used a  
215 two-pronged approach: (1) single sensor signal analysis based on feature extraction and  
216 unsupervised machine learning, and (2) array-based analysis using all the sensors of AGIR and  
217 classic multi-channel correlation algorithms. Together, these methods provide complementary  
218 insights into the acoustic behavior of the storm, capturing both local signal characteristics and  
219 spatial coherence across sensors.

220 For the single-station analysis, infrasound data recorded at the AGIR sensor (Figure 2) was  
221 segmented into 30-minute windows, and a set of time-frequency features was extracted to  
222 characterize the signal dynamics (Supplementary Material). These features describe how energy  
223 and frequency content evolve over time, providing insights into the structure of the infrasound  
224 signal. Parameters such as spectral centroid and spectral rolloff are standard descriptors in acoustic  
225 signal analysis and are suitable here because they effectively capture shifts in dominant frequency  
226 produced by lightning-generated acoustic waves or the passage of pressure disturbances, while  
227 spectral flux highlights changes in broadband acoustic energy (Pásztor et al., 2023). Spectral  
228 entropy reflects the complexity of the frequency distribution, which increases during turbulent  
229 atmospheric conditions, and the zero-crossing rate, mean, and variance of the power spectrum  
230 summarize overall activity and variability. This feature set provides a compact representation of  
231 the signal suitable for unsupervised machine-learning approaches such as clustering, techniques  
232 widely used in data mining to identify patterns in multidimensional time-frequency data (e.g.,  
233 Coates and Ng, 2012), and allows us to distinguish physically interpretable stages of storm-induced  
234 changes in the infrasound wavefield.

235 The extracted features were used as input for K-Means clustering (MacQueen, 1967), an  
236 unsupervised machine learning algorithm that partitions data into a predefined number of groups.  
237 K-Means minimizes within-cluster variance by iteratively assigning feature vectors to the nearest  
238 cluster centroid and updating the centroids based on the grouped data. This clustering method  
239 enables the identification of distinct acoustic patterns in the signal (e.g. Pásztor et al., 2023),  
240 offering a data-driven way to segment the storm’s infrasound profile without requiring prior labels  
241 or assumptions. Prior to clustering, the features were standardized using z-score normalization, to  
242 ensure comparable scaling across variables. The optimal number of clusters was determined using  
243 the elbow method, which evaluates within-cluster variance as a function of cluster number  
244 (Supplementary Material). To select the most informative features, we applied covariance pruning,  
245 and the temporal evolution of the features was visualized to ensure meaningful representation. This  
246 procedure resulted in six clusters, providing a balanced representation of the infrasound dynamics  
247 while avoiding over-segmentation or overfitting. By combining multiple features in the clustering,  
248 this method captures the evolving acoustic states of the storm in a compact, interpretable form.

249 In parallel with the single-station analysis, we also applied the Progressive Multi-Channel  
250 Correlation (PMCC) method, as implemented in the DTK-PMCC software (Cansi and Le Pichon,  
251 2008; Le Pichon et al., 2010) to detect and analyze coherent acoustic signals across an infrasound  
252 array. The PMCC method targets signals generated by atmospheric sources such as lightning (i.e.,  
253 associated thunders) or other pressure disturbances, operating in the low-frequency range of 0.7 to

254 7 Hz. It is specifically suited for mini-array configurations, where signal coherence between  
255 closely spaced sensors can be exploited for precise signal detection and characterization.

256 The PMCC algorithm was implemented using a multi-resolution configuration following the  
257 standardization proposed by Garcés (2013), with window lengths and frequency bands arranged  
258 in third-octave bands. A total of 19 frequency bands were used, covering 0.1-7 Hz. Window  
259 lengths decrease logarithmically with frequency, ranging from 258 s in the lowest band to 4 s in  
260 the highest band. A 10% time step was applied (corresponding to 90% overlap between  
261 consecutive windows), and this scheme repeats every decade. Within each time-frequency  
262 segment, cross-correlations are computed between all sensor pairs to identify coherent wavefronts,  
263 signals that exhibit consistent arrival times across the array. From these detections, PMCC  
264 estimates several key propagation parameters, including backazimuth (the direction of arrival),  
265 horizontal trace velocity, amplitude, duration, and dominant frequency. This approach is  
266 particularly effective in noisy environments and enables the discrimination of storm-generated  
267 infrasound from background signals or unrelated acoustic sources. The algorithm's output consists  
268 of a time-frequency map of signal detections enriched with physical metadata, allowing for  
269 detailed interpretation of the storm's acoustic footprint and its temporal evolution.

### 270 3.3 Satellite Observations

271 We also incorporated data from the Meteosat Third Generation (MTG) satellite system (Holmlund  
272 et al., 2021), specifically from its Lightning Imager (LI) sensor (Viticchie et al., 2020). The MTG  
273 satellites operate in geostationary orbit at approximately 36,000 km altitude, providing continuous  
274 observations over Europe, Africa, and surrounding waters. The Lightning Imager detects cloud-  
275 to-cloud, cloud-to-ground, and intra-cloud lightning flashes using four cameras that collectively  
276 cover 86% of the Earth's visible disc from the satellite's perspective.

277 For this study, we used Level 2 group data, which includes the geographical coordinates and timing  
278 of each detected flash. The MTG Lightning Imager detects total lightning (cloud-to-cloud and  
279 cloud-to-ground) optically at 777 nm, with 4.5 km pixel resolution at the sub-satellite point and  
280 1 ms frame rate (Holmlund et al., 2021; Kokou, 2023). Level-2 achieves detection efficiencies of  
281 ~80-90%, capturing even weak flashes reliably, with false alarm rates <0.3 (Enno et al., 2025).  
282 Flash geolocation uncertainty reaches 5-10 km near the edge of the instrument's field of view,  
283 where off-nadir viewing geometry amplifies parallax effects (Bližňák & Sokol, 2026). By mapping  
284 these detections, we were able to analyze the spatial distribution and temporal evolution of the  
285 storm's lightning activity. The dataset also offered insights into the storm's intensity and structure,  
286 complementing other meteorological observations.

287 Associations between infrasound detections and lightning flashes detected by MTG within 50 km  
288 of the AGIR infrasound station were investigated by assuming direct-path acoustic propagation  
289 and a correspondence between infrasound time-of-arrival and the MTG lightning discharge time  
290 (after Assink et al., 2008):

$$291 t = t_{\text{MTG}} + d/c + \Delta t,$$

292 where  $d$  is the distance between the lightning discharge and the infrasound station,  $c = 340\text{m/s}$ ,  
293 and  $\Delta t = \pm 10\text{s}$  accounts for timing uncertainty associated with the simplified propagation

294 assumption. In particular, infrasound travel time from thunder sources can vary due to atmospheric  
295 temperature and wind variations along the propagation path, which affect the effective sound speed  
296 and may introduce deviations from the assumed constant-velocity, straight-path propagation.  
297 Additionally, a maximum angular deviation of  $10^\circ$  between the observed infrasound backazimuth  
298 and the MTG-derived backazimuth is permitted for an association to be accepted.

### 299 **3.4 GNSS Data**

300 The use of GNSS technology for atmospheric monitoring provides a powerful tool for analyzing  
301 extreme weather events. Beyond its well-known applications in navigation, timing, positioning  
302 and crustal dynamics (Nistor et al., 2021a; Nistor et al., 2021b), GNSS has become a reliable  
303 method for sensing tropospheric water vapour, an essential driver of weather systems and a key  
304 variable in forecasting models (Guerova et al., 2016; Vaquero-Martínez and Antón, 2021). Over  
305 the past two decades, ground-based GNSS networks in Europe have contributed significantly to  
306 operational meteorology by providing near real-time estimates of atmospheric water vapour,  
307 aiding in the detection and tracking of severe weather, including heavy rainfall and storms  
308 (Karabatić et al., 2011; Priego et al., 2017; Jones et al., 2020). These high-resolution observations  
309 have proven valuable for both nowcasting and validating numerical weather prediction models  
310 (Wilgan et al., 2015; Bosy et al., 2012; Awange, 2012).

311 In this study, GNSS data were collected from several networks (Figure 2), including the  
312 International GNSS Service (IGS, Johnston et al., 2017), the EUREF Permanent Network (EPN,  
313 Bruyninx et al., 2012), the Romanian Position Determination System (ROMPOS, Iliescu et al.,  
314 2019), and GEOPONTICA (Dimitriu et al., 2017). A total of 37 permanent GNSS stations were  
315 analyzed over a 30-day period, with the rainiest interval selected at the midpoint of the study  
316 period. These stations provide high-quality, continuous observations critical for atmospheric  
317 monitoring.

318 The data were processed using a double-differenced, ionosphere-free combination of L1 and L2  
319 carrier phases. This approach helps minimize errors such as ionospheric delays, satellite clock  
320 biases, and other common atmospheric effects. The resulting Zenith Tropospheric Delay (ZTD)  
321 values were then corrected using the Vienna Mapping Functions 3 (VMF3, Landskron et al., 2018),  
322 which improves the accuracy of ZTD by accounting for variations in the troposphere's atmospheric  
323 conditions. Once the ZTD was refined, it was converted into integrated precipitable water vapor  
324 (PWV) using surface meteorological data (temperature and pressure) from co-located weather  
325 stations, following the method outlined by Bosy et al. (2012). This process allowed for the  
326 derivation of high-resolution atmospheric water vapor content, critical for analyzing the dynamics  
327 of the extreme storm event over the Black Sea. By combining GNSS-derived PWV with data from  
328 other observational sources, the study captured the temporal and spatial variations in atmospheric  
329 moisture, offering valuable insights into the storm's development and intensity.

### 330 **3.5 Meteorological Data**

331 To compare the infrasound signals captured during the Black Sea extreme storm event, we  
332 extracted meteorological data from the open-access ERA5 reanalysis dataset, produced by the  
333 European Centre for Medium-Range Weather Forecasts (ECMWF). This dataset provides a  
334 comprehensive record of global weather conditions from 1950 to the present (Hersbach et al.,

335 2023). ERA5 combines observational data and advanced numerical models to generate relatively  
336 high-resolution atmospheric parameters compared with earlier global reanalyses, including  
337 precipitation (Figure 1), wind speed, and wave height. ERA5 has been extensively validated (Jiao  
338 et al., 2021; Wu et al., 2022; Soci et al., 2024) and is widely used in studies of storm evolution and  
339 precipitation dynamics (e.g. Dullart et al., 2020; Tiberia et al., 2021; Price et al., 2025), making it  
340 a suitable choice for the mesoscale processes examined here.

341 For our study, the ERA5 data was used to track the meteorological context of the storm, offering  
342 insights into the intensity of precipitation, the evolution of wind patterns, and the development of  
343 oceanic wave heights. With a temporal resolution of 1 hour and spatial resolution of  $0.25^\circ \times 0.25^\circ$ ,  
344 ERA5 allows for a mesoscale comparison of the storm's meteorological characteristics over time.  
345 While its spatial averaging cannot resolve localized convective-scale precipitation, it provides a  
346 vital benchmark for qualitative comparisons and for testing multi-sensor monitoring potential.  
347 These comparisons help us understand the storm's dynamics and assess its impact, further  
348 enhancing the interpretation of infrasound signals and aiding in future storm prediction and  
349 monitoring efforts. The open-access nature of ERA5 ensures broad accessibility, contributing to  
350 the transparency and reproducibility of our storm analysis (Copernicus Climate Change Service,  
351 Climate Data Store, 2023).

## 352 **4. Results**

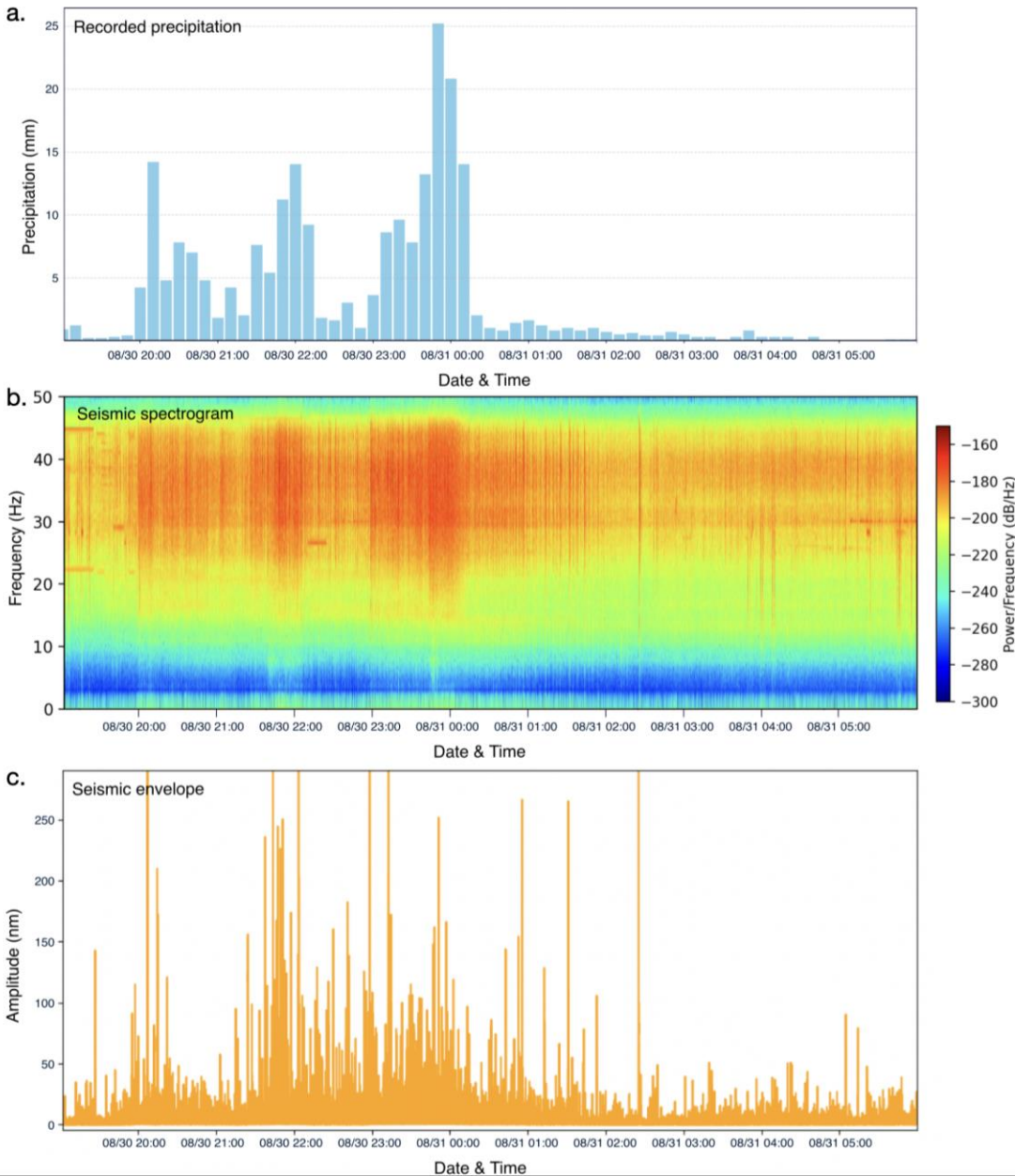
### 353 **4.1 Seismic signatures of storm evolution**

354 High frequency ( $>30$  Hz) analysis of seismic noise reveals strong signals during periods of intense  
355 rainfall (Figure 4). Specifically, the displacement envelope at station MANR and its spectrogram  
356 for 30 August, 12:00 UTC to 31 August, 06:00 UTC (Figures 4b, c) reveal strong signal around  
357 midnight, when recorded precipitation exceeded 20 mm per 10 minutes. Similar temporal patterns  
358 in the seismic spectrogram were also visible when compared with hourly precipitation levels from  
359 ERA5, indicating that the high amplitude of energy observed above 30 Hz is most plausibly  
360 generated by raindrop impacts.

361 However, this correspondence is not uniform across all rainfall episodes. While the main  
362 precipitation maximum on 30-31 August produces a clear and sustained seismic response, several  
363 lower-intensity precipitation pulses show a much weaker or no recognizable signature in either the  
364 seismic envelope or spectrogram. This behaviour is consistent with previous work (e.g.,  
365 Rindraharisaona et al., 2022), which demonstrates that only rainfall above a certain intensity, or  
366 involving sufficiently large drops, generates impact forces strong enough to be detected by  
367 broadband seismometers. Our observations therefore reflect both strong positive correlations  
368 during intense rainfall and the lack of seismic expression for weaker precipitation. This selective  
369 sensitivity supports the interpretation that high-frequency seismic noise can reflect strong rainfall  
370 peaks but is less responsive to light or moderate precipitation, an important nuance when  
371 interpreting multi-sensor relationships in this study.

372 Anthropogenic seismic noise is typically strongest at low to mid frequencies ( $<25$  Hz), where day-  
373 night variations reflect traffic, human activity, and transient signals from machinery, while higher-  
374 frequency bands (25-45 Hz) may include periodic contributions from rotating equipment (e.g.,  
375 Gross & Ritter, 2008; Diaz et al., 2017). The bandwidth targeting rainfall in this case is between

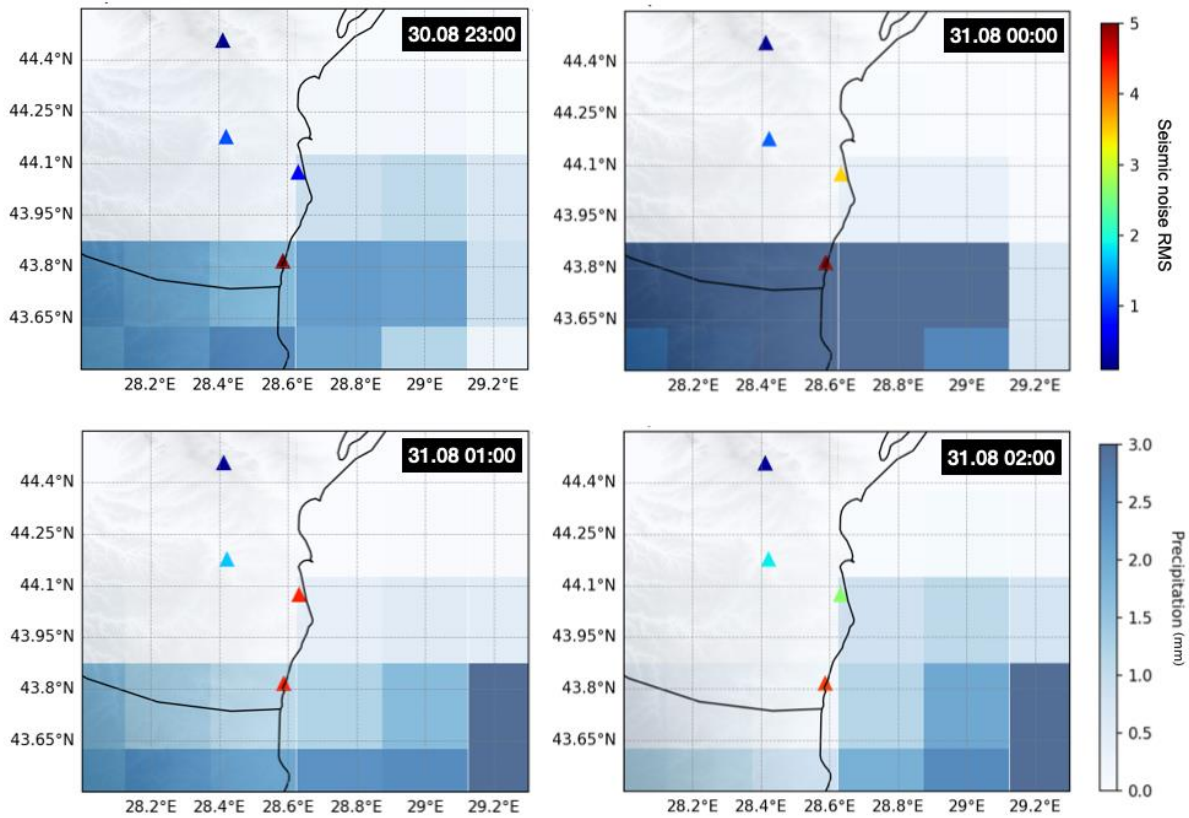
376 30-50 Hz, which is above the dominant frequency content of most anthropogenic sources and  
377 overlaps with raindrop-impact energy documented in recent rainfall-seismic studies.



378  
379 *Figure 4. High frequency (30-50Hz) observations of the storm at station MANR. a. Time series of total*  
380 *precipitation every 10 minutes from the ANM station at Mangalia b. Spectrogram of the seismic time series*  
381 *for station MANR. c. Envelope of the displacement seismogram at station MANR.*

382 To visualise the signature of the storm passing over the network of broadband seismic stations in  
383 the coastal area, we also plotted the hourly precipitation values with the hourly root-mean-square  
384 amplitudes of the high-frequency (>30 Hz) seismic velocity envelopes recorded at seismic stations.  
385 Figure 5 shows four snapshots of hourly plots of gridded precipitation data from ERA5, which  
386 have a lower amplitude than point measurements at the Mangalia station, due to the averaging over

387 the grid block. This figure presents a temporal coincidence between changing precipitation patterns  
 388 from ERA5 data and the amplitudes of high-frequency seismic noise. This observation further  
 389 supports the likelihood of a causal relationship. These high-frequency seismic signals could  
 390 potentially be explored as a near real time indicator of intense rainfall events, providing a  
 391 conceptual basis for a simple streaming detection approach.



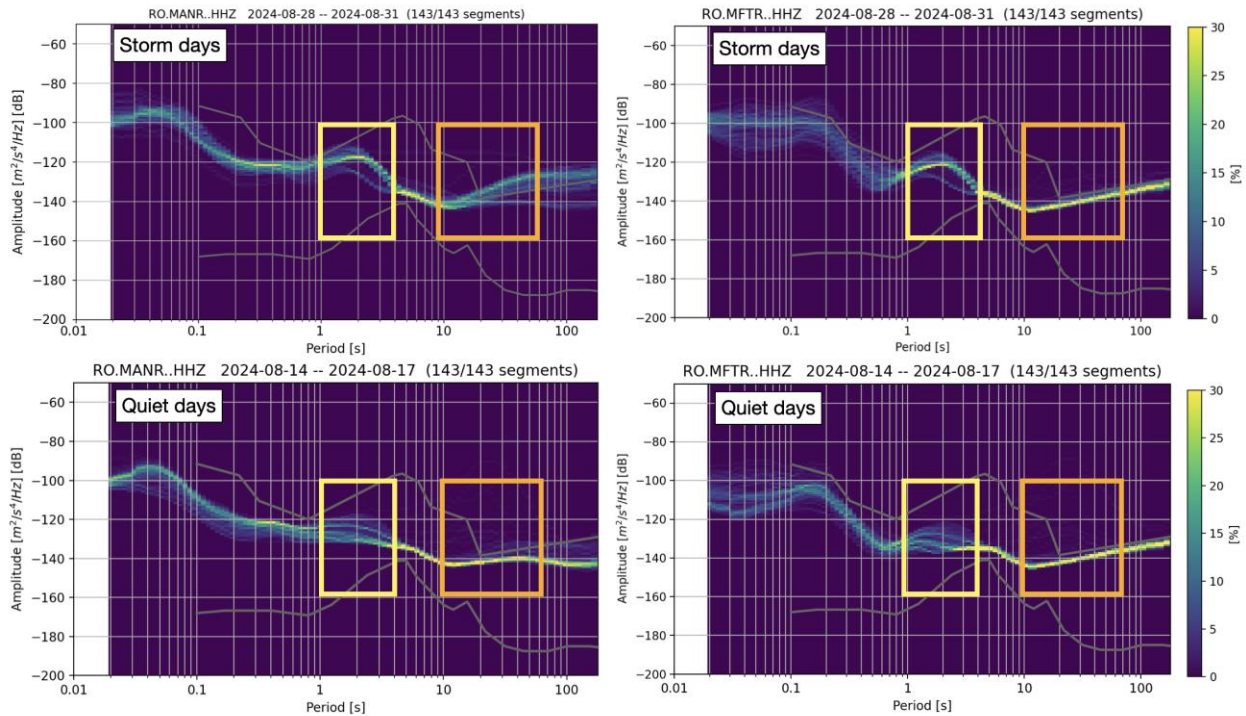
392  
 393 *Figure 5. Distribution of hourly RMS of high pass filtered (>30 Hz) seismograms and precipitation data.*  
 394 *Colours indicate hourly RMS amplitude of velocity envelopes filtered 30-50 Hz. Background coloured*  
 395 *grid indicates the total precipitation (mm) from ERA5 data.*

396 The analysis of the microseismic noise frequency band is closely linked to the interaction between  
 397 ocean waves and the seafloor, which is influenced by storm conditions. To assess the storm's  
 398 impact, we analyze the PPSD (Probabilistic Power Spectral Density) of noise recorded at several  
 399 stations during both storm and quiet days, using the latter as a baseline. Figure 6 shows examples  
 400 of PPSD at stations MANR and MFTR (Figure 2), revealing differences in PSD amplitudes across  
 401 the primary and secondary microseismic bands. These differences indicate the presence of high-  
 402 intensity wind-driven waves and swell energy in the sea.

403 The secondary microseismic band, in particular, shows a significant rise in amplitude during  
 404 storms, consistent with established mechanisms linking storm-driven wave activity and seafloor  
 405 pressure fluctuations (Figure 3) to enhanced secondary microseism generation, while local factors  
 406 such as bathymetry or wave direction may modulate the response (Bromirski et al., 2002; Ebeling

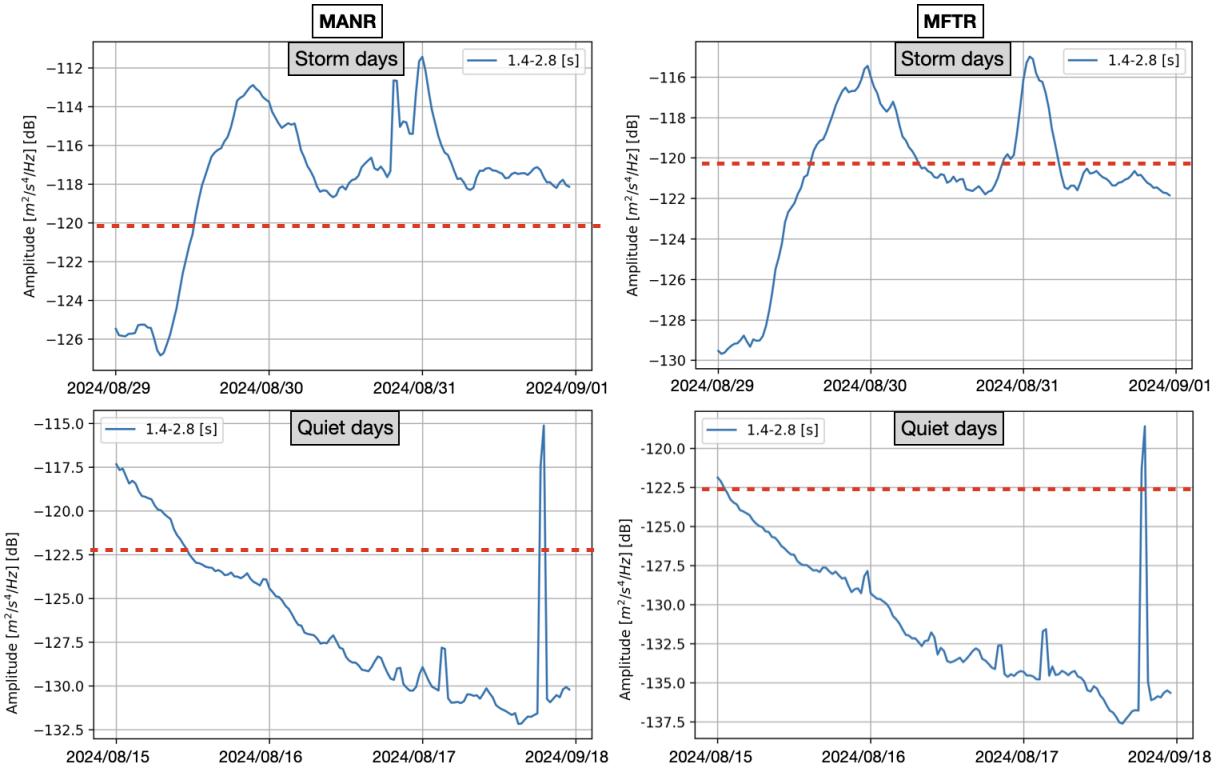
407 et al., 2012; Arduin et al., 2019). On quiet days, the PSD remains consistently lower, typically  
 408 staying below the -120 dB threshold. This stark contrast emphasizes the role of atmospheric  
 409 conditions in modulating seismic noise, with storms causing a notable increase in energy across  
 410 both frequency bands. The temporal evolution of the PSD values (Figure 7) further highlights the  
 411 storm's impact, with fluctuations corresponding to changes in environmental factors, reinforcing  
 412 the connection between storm activity and the observed seismic signals.

413



414  
 415 *Figure 6. Probabilistic Power Spectral Density (PPSD) plots for two seismic stations near the Black Sea*  
 416 *coast capturing the target storm signal in the microseismic bandwidths (marked with rectangles). The top*  
 417 *panels show the PPSD distributions across frequencies, indicating the probability of power spectral*  
 418 *density values in percentage for days including the Black Sea storm. The bottom panels show PPSD for*  
 419 *days with no recorded events.*

420 Anthropogenic seismic noise does not significantly affect the microseismic band (0.1-1 Hz).  
 421 Human-generated vibrations predominantly occupy frequencies above 1 Hz, while long-period  
 422 microseisms are produced by ocean wave interactions and are coherent over large distances. The  
 423 temporal evolution of the microseismic energy observed in this study matches changes in wave  
 424 state associated with the storm rather than any local activity. Similar to the findings of Gross &  
 425 Ritter (2009), the sub-Hz frequency range is dominated by natural sources, with anthropogenic  
 426 contributions being negligible.



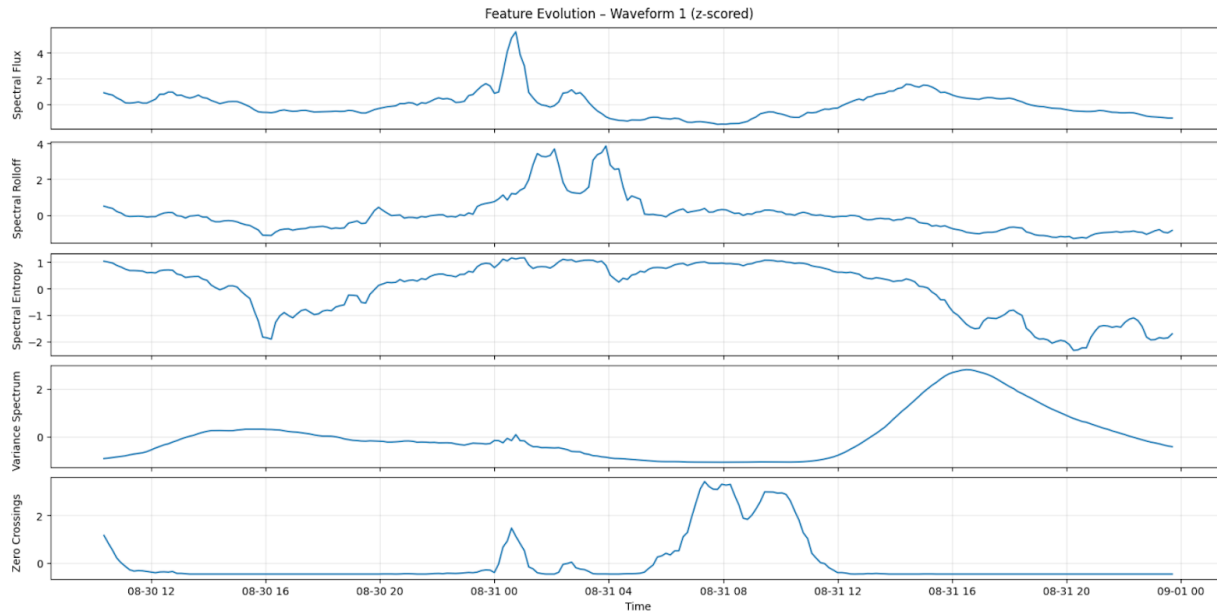
427

428 *Figure 7. Temporal PSDs for two seismic stations near the Black Sea Coast in the secondary microseismic*  
 429 *band showing significantly higher values (>-120 dB) during stormy days compared to days without*  
 430 *recorded precipitation.*

## 431 4.2 Infrasonic and satellite lightning observations

### 432 4.2.1 Single-station feature extraction

433 The evolution of time-frequency features over the duration of the Black Sea storm revealed distinct  
 434 patterns in the infrasonic signal (Figures 8 and 9). Centroid and rolloff show parallel behavior  
 435 because they are both frequency-domain descriptors tied to the distribution of spectral energy, and  
 436 so both respond strongly to the same uplift in energy during the storm's peak. Spectral flux, by  
 437 contrast, quantifies inter-frame spectral change, so its peak occurs where the spectrum transitions  
 438 most rapidly, even when that does not coincide with the maximum absolute energy (e.g. Pásztor  
 439 et al., 2023). Finally, the zero-crossing rate reflects time-domain volatility, not spectral shape,  
 440 which explains its distinct pattern, such as the storm's later stages may introduce broadband  
 441 turbulence or noise components that boost zero crossings independently of the spectral shifts  
 442 visible in the first two panels. While the individual features varied over time, it is the combination  
 443 of these features through K-means clustering that effectively identifies the time frame  
 444 corresponding to the main precipitation episode. Zero-crossings exhibited more variable patterns,  
 445 reflecting high-frequency fluctuations, but the joint clustering of all features robustly captures the  
 446 timing of the storm's most intense phases.

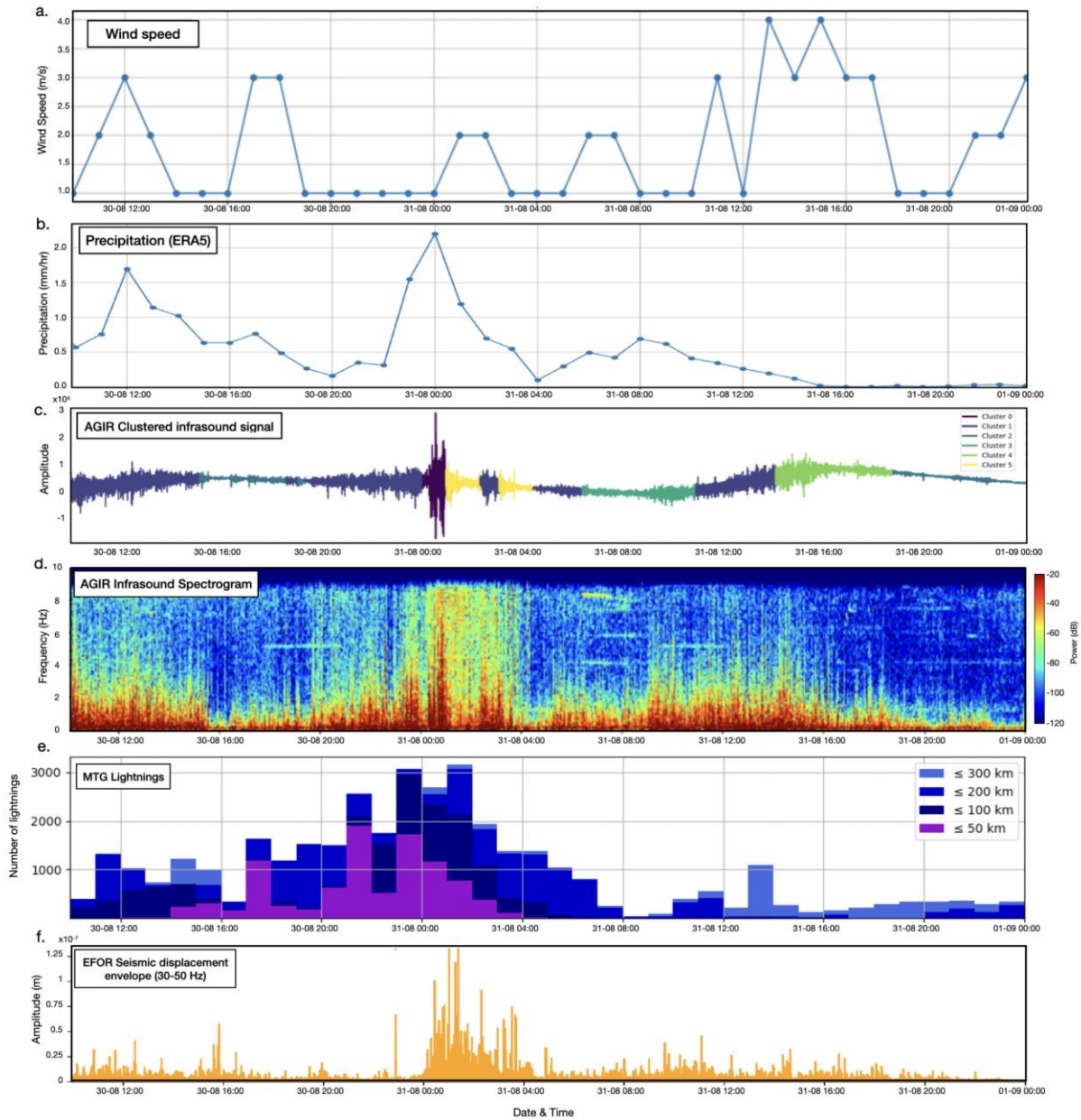


447

448 *Figure 8. Time-frequency feature analysis for the single-station infrasound signal recorded at AGIR during*  
 449 *the Black Sea Storm.*

450 K-means clustering separated the acoustic data into six groups with distinct spectral and amplitude  
 451 characteristics (Figure 9). These clusters highlight acoustic states that may relate to different  
 452 environmental conditions during the monitoring period. For example, Cluster 0 coincides with  
 453 periods of intense precipitation and stronger winds, and also aligns with enhanced lightning  
 454 activity, suggesting a link with the most energetic phases of the convective system. Cluster 1  
 455 captures intervals with moderate amplitudes but persistently elevated background acoustic levels,  
 456 without corresponding rainfall or wind peaks, and with comparatively reduced lightning  
 457 occurrence. Cluster 2 reflects calmer conditions with low amplitudes and little or no precipitation  
 458 and minimal lightning activity. Transitional patterns also arise, such as Cluster 3, which appear  
 459 before intervals grouped in Cluster 1 and mark intermediate acoustic activity. Overall, the  
 460 clustering approach demonstrates that combining multiple features reveals consistent acoustic  
 461 regimes and can help differentiate environmental conditions, without relying on any single  
 462 parameter.

463 Interestingly, the spectral content of the infrasound signal showed similarities to seismic signal  
 464 envelopes, particularly in the high frequency ranges (Figure 9), which may suggest a connection  
 465 between the atmospheric pressure waves detected by infrasound and the ground vibrations  
 466 captured by seismic instruments. When considered alongside the temporal evolution of lightning  
 467 activity, this overlap implies that both seismic and infrasound signals could be complementary in  
 468 capturing different aspects of storm dynamics, with seismic signals reflecting ground vibrations  
 469 and infrasound capturing the atmospheric processes, and lightning indicating convective intensity.



470  
 471 *Figure 9. Clustering results of infrasound signals recorded at AGIR from the August Black Sea storm event*  
 472 *compared with precipitation data and seismic signal from EFOR station. a. Wind speed per hour measured*  
 473 *at ANM meteorological station Constanta; b. Average precipitation data from  $1^{\circ} \times 1^{\circ}$  around AGIR. c. Raw*  
 474 *infrasound signal recorded at the AGIR sensor during the period of August 30–31, 2024, with different*  
 475 *segments color-coded according to the cluster they belong to, based on K-means clustering of 30-minute*  
 476 *time-frequency feature windows. d. The corresponding spectrogram generated using Blackman windowing*  
 477 *with 128 samples and 70% overlap; e. Number of lightnings detected by the MTG satellite. f. Seismic*  
 478 *displacement envelope at station EFOR, filtered between 30–50 Hz.*

479

480

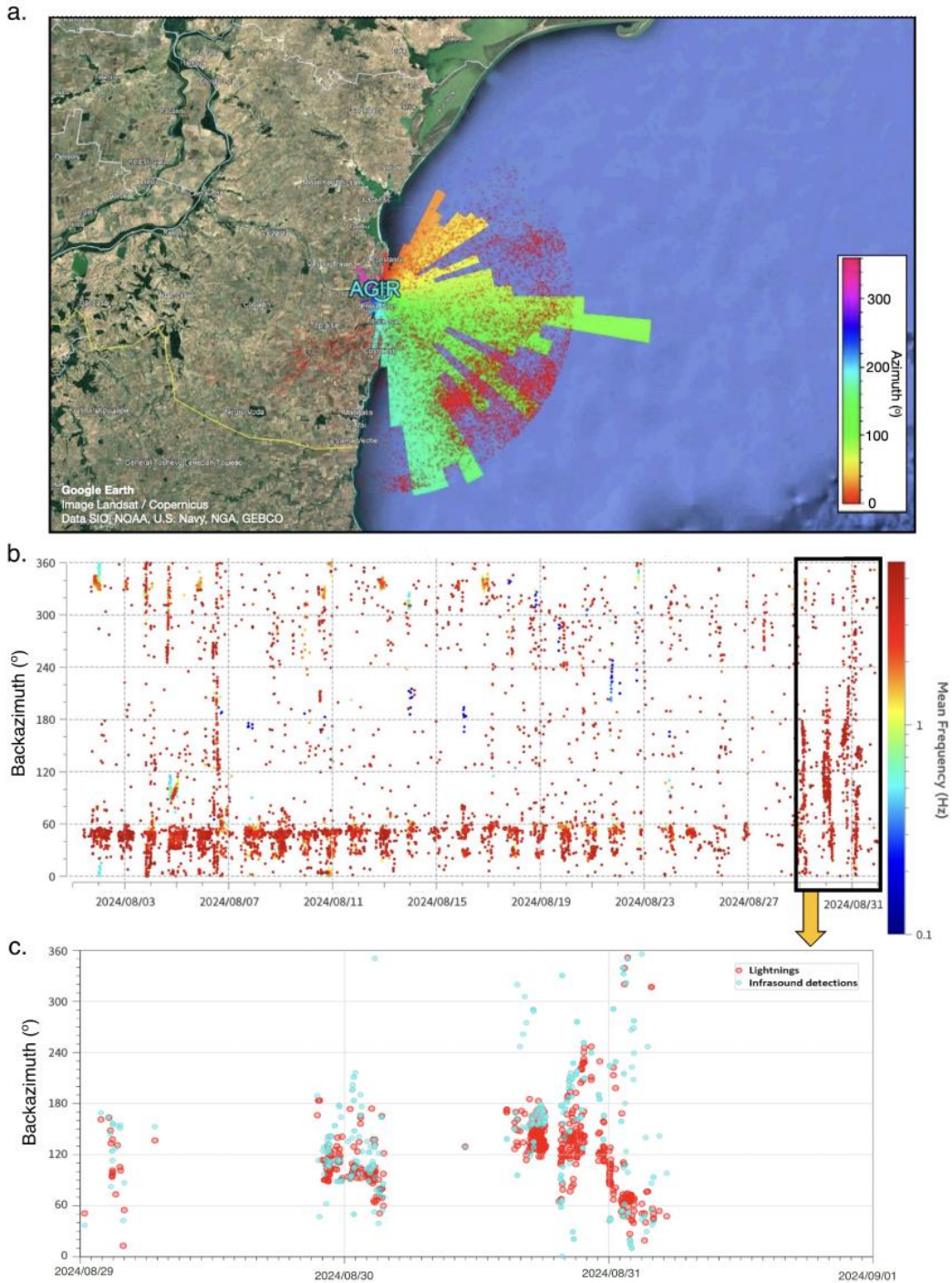
481

## 482 4.2.2 Array analysis and lightning detection

483 Using multiple sensors from the AGIR infrasound array with the PMCC algorithm allowed us to  
484 isolate coherent infrasound signals and estimate their propagation parameters, such as backazimuth  
485 and arrival times, across the sensor network. Nearly 11,000 lightning flashes were detected by the  
486 MTG Lightning Imager within 50 km of the AGIR station during the Black Sea storm (Figure  
487 10a), providing a dense reference set for comparison. Within the relevant 0.6-7 Hz frequency band,  
488 approximately 1,100 infrasound detections were identified. These signals primarily consisted of  
489 long-duration wave trains with frequent amplitude peaks and short-lived disturbances  
490 characteristic of lightning-generated infrasound. Their dominant frequency was around 3 Hz, and  
491 amplitudes ranged from 0.01 to 3.4 Pa (Figure 10b).

492 A subset of the infrasound detections could be confidently associated with individual lightning  
493 discharges based on temporal alignment and backazimuth consistency. Overall, we were able to  
494 associate 6.4% of lightning flashes with infrasound detections at AGIR (Figure 10c). This level of  
495 correspondence is reasonable given that only a subset of lightning discharges radiate infrasound  
496 efficiently and that propagation strongly depends on altitude, source geometry, and atmospheric  
497 conditions. Nevertheless, these coincident detections demonstrate that lightning-generated  
498 infrasound was clearly recorded during the storm and that the PMCC-derived acoustic signatures  
499 provide valuable insight into the evolution of electrical activity and storm dynamics.

500 Anthropogenic noise sources, such as wind turbines (e.g., Jakobsen, 2005), industrial machinery  
501 (Gastmeier and Howe, 2008), and road traffic (Grafkina et al., 2019), are well-documented  
502 challenges for infrasound studies because they often generate persistent, periodic, or tonal signals  
503 that can mask natural atmospheric phenomena. The AGIR infrasound array used here is located in  
504 a semi-rural setting, distant from major roads and industrial facilities, which reduces the likelihood  
505 of local anthropogenic contamination. Several independent lines of evidence indicate that such  
506 contamination is negligible in this case study. First, the strongest infrasound signatures occurred  
507 during night-time hours, when human activity is minimal. Second, both the clustering and PMCC  
508 analyses identify transient signals with energy peaking around  $\sim 3$  Hz, which contrasts sharply with  
509 the more continuous or harmonic spectral patterns typically produced by anthropogenic sources.  
510 Third, the temporal alignment of these acoustic signatures with independent observations of  
511 lightning and precipitation provides ~~strong~~ confirmation that the detected infrasound variability is  
512 storm-related rather than anthropogenic in origin.

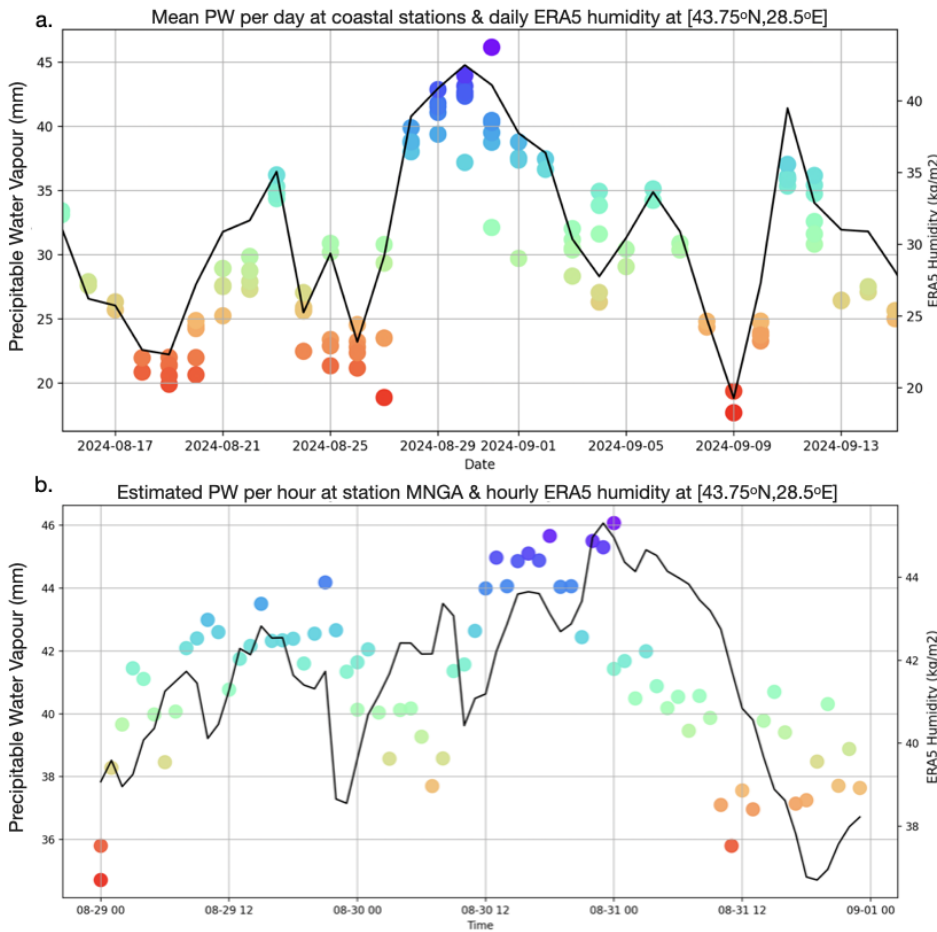


513

514 *Figure 10. a. Polar histogram of infrasound detections from the AGIR station, displayed with © Google*  
 515 *Earth, along with the locations of lightning strikes detected by the MTG Lightning Imager system for the*  
 516 *period from 29-31st of August 2024. The geographical position of the AGIR infrasound station is also*  
 517 *shown on the map. b. diagram of high-frequency detections from the AGIR infrasound station between 1-*  
 518 *31st of August 2024. c. Associations between events detected by the AGIR infrasound array and the MTG*  
 519 *satellite database for 29-31st of August 2024.*



548 buildup of PWV, reaching values greater than 44 mm just a few hours before the storm event. This  
 549 rapid increase in PWV suggests that the accumulation of atmospheric moisture may precede to  
 550 extreme weather events, such as intense rainfall and storms. This observation aligns with known  
 551 atmospheric dynamics, where a significant increase in water vapor content precedes heavy  
 552 precipitation, highlighting the potential usefulness of GNSS-based PWV monitoring for studying  
 553 pre-storm atmospheric moisture variability. The general rising trend toward the event is present in  
 554 both GNSS-based and ERA5 reanalysis datasets, although some minor fluctuations are not  
 555 matched. After the storm, the GNSS PWV drops sharply while ERA5 maintains elevated values  
 556 for several hours. These differences show that GNSS can resolve rapid, real-time atmospheric  
 557 changes that may be blurred in large-scale weather model products.



558

559 *Figure 12. Comparison of GNSS-derived precipitable water vapor (coloured circles) with independent*  
 560 *humidity data (black line) from ERA5's total column vertically integrated water vapor parameter. a. Mean*  
 561 *PWV values per day at selected GNSS stations (CONB, HARI, MNGA, MNGL, MNGM, TUZL) alongside*  
 562 *daily averaged ERA5 humidity. b. Estimated PWV values per hour at the MNGA GNSS station compared*  
 563 *with hourly ERA5 humidity at the 43.75°N, 28.5°E grid point. In both panels, GNSS data points are*  
 564 *represented by colored circles where the color scale corresponds to the PWV magnitude, consistent with*  
 565 *the vertical axis.*

## 566 5. Discussion

567 Storm evolution, in the meteorological sense, describes the sequence of processes from pre-storm  
568 atmospheric moisture accumulation to convective initiation, peak rainfall, electrical activity, and  
569 the associated marine response along coastal areas. The multi-sensor dataset used here captures  
570 these different stages: GNSS-PWV documents the build-up of column water vapor before  
571 convective onset, infrasound detects lightning-generated acoustic waves and pressure disturbances  
572 during the mature convective phase, high-frequency seismic noise reflects the timing and spatial  
573 progression of intense rainfall at the surface, microseisms respond to storm-driven changes in sea  
574 state, and ERA5/MTG provide the mesoscale structure that ties these geophysical signals together.  
575 By observing the same storm through these complementary physical pathways, we can outline a  
576 more detailed picture of how the storm developed, intensified, and decayed than is possible from  
577 individual datasets.

578 The integration of infrasound, seismic, and GNSS data in monitoring the extreme storm event over  
579 the Black Sea provides valuable insights into the dynamics of storm behavior and illustrates the  
580 potential of repurposing non-conventional sensors for meteorological analysis. Infrasound data,  
581 for instance, revealed a clear acoustic signature of lightning activity, with signals detected in the  
582 range of 0.6 to 7 Hz corresponding to electrical discharges. The high frequency of infrasound  
583 detections (around 1,100) suggests that it may provide useful information for tracking storm-  
584 related phenomena, particularly lightning, which is difficult to capture with traditional methods.  
585 However, the signals did not always perfectly align with lightning strikes, indicating that other  
586 factors, such as the movement of storm systems or variations in atmospheric conditions, may  
587 influence infrasound signatures. This suggests that refining the correlation between infrasound  
588 signals and lightning activity could be an avenue for future research, particularly in cases of sparse  
589 lightning or in remote regions.

590 Seismic data alone also showed a strong connection between high-frequency seismic noise and  
591 heavy rainfall, supporting previous studies that linked seismic signals to rainfall intensity. The  
592 distinction between high-frequency and low-frequency seismic noise is particularly noteworthy.  
593 Increases in high-frequency seismic noise occurred during intense precipitation, while low-  
594 frequency signals were associated with wave height and storm-driven winds. This suggests that  
595 different seismic frequencies capture distinct storm dynamics, with high-frequency signals  
596 reflecting localized rainfall impacts and low-frequency signals tied to broader atmospheric and  
597 oceanic interactions. This dual-frequency approach provides a more nuanced interpretation of  
598 seismic data in storm monitoring, highlighting its complexity.

599 A key finding of this study is that K-means clustering of multiple acoustic features, including  
600 spectral centroids, roll-off, flux, and zero-crossing rate, effectively segmented the infrasound  
601 record into distinct storm phases. This approach proved more robust than relying on any single  
602 feature, as the combination captured the complex, evolving nature of the storm's acoustic signature.  
603 For instance, the identified clusters delineated periods of intense precipitation, elevated  
604 background acoustic levels, and calm intervals, providing a data-driven overview of the storm's  
605 progression. The fact that these acoustically defined phases align with independent meteorological  
606 observations, such as rainfall peaks, confirms that the infrasound signal variability is a direct  
607 response to the storm's atmospheric dynamics.

608 Furthermore, the observed spectral similarity between the infrasound signals and high-frequency  
609 seismic envelopes suggests a coupled seismo-acoustic response to the storm. This implies that the

610 same atmospheric forcing, such as pressure fluctuations from rainfall and wind, generates  
611 complementary signals in the atmosphere (infrasound) and the ground (seismic waves). Our  
612 findings are consistent with other studies of intense weather systems, where coupled microbarom-  
613 microseism signals have been shown to track storm structure and evolution (e.g., Butler & Aucan,  
614 2018; Smirnov, 2021). The coherent acoustic and seismic responses to atmospheric-oceanic  
615 pressures, as also documented in Distributed Acoustic Sensing studies (Taweessintananon et al.,  
616 2023) and surf studies (Francoeur et al., 2025), reinforce the interpretation of a shared source  
617 mechanism. Therefore, a major and logical next step is to move beyond analyzing these datasets  
618 in parallel and to perform joint clustering of seismo-acoustic data (e.g. Floroiu et al., 2025). Such  
619 an integrated approach could unlock a more comprehensive, multi-physics understanding of storm  
620 dynamics by simultaneously characterizing the coupled atmospheric and ground-borne wavefields.

621 The temporal variations observed in GNSS-derived integrated precipitable water vapor provide  
622 valuable insights into atmospheric moisture dynamics before extreme weather events. The  
623 pronounced increase in PWV, particularly in the days leading up to and during the storm, supports  
624 the link between elevated atmospheric water vapor and precipitation. Notably, the PWV buildup  
625 starting roughly three days before the extreme rainfall suggests that rising moisture levels in the  
626 troposphere were observed prior to the intense precipitation in this event. Even stations located up  
627 to 130 km inland, such as HAR1, recorded similar PWV trends, indicating that GNSS stations  
628 outside direct storm zones can still provide crucial atmospheric data. Hourly PWV trends further  
629 revealed a rapid increase several hours before precipitation, with values exceeding 44 mm/hr,  
630 highlighting the accumulation of moisture just before heavy rainfall. These findings align with the  
631 notion that increasing atmospheric moisture acts as a precursor to intense precipitation,  
632 highlighting the potential of GNSS-based PWV monitoring for tracking moisture and  
633 understanding short-term atmospheric fluctuations.

634 The integration of GNSS, infrasound, and seismic data provides a more comprehensive  
635 understanding of storm dynamics than any single data source alone. The synergy between these  
636 diverse sensor types allows for the detection of atmospheric moisture, lightning activity, rainfall-  
637 induced seismic signals, and storm-driven oceanic interactions. Future research should focus on  
638 refining unsupervised learning algorithms for infrasound and seismic signal classification,  
639 optimizing joint clustering techniques, and improving the integration of these data sources to  
640 enhance storm forecasting and early-warning systems. This case study highlights the potential of  
641 multi-sensor observations to enhance our understanding of extreme storm behavior and support  
642 the development of future early-warning strategies.

## 643 **6. Conclusions**

644 This study presents a comprehensive analysis of a record-breaking storm over the Black Sea, using  
645 a combination of GNSS, infrasound, and seismic data to capture the dynamics of extreme weather  
646 events. Our findings underscore the power of multi-sensor networks in enhancing the  
647 understanding of storm behavior, particularly in the context of atmospheric moisture, lightning  
648 activity, and storm-induced seismic signals. GNSS-derived integrated precipitable water vapor  
649 indicates a clear buildup of atmospheric moisture hours before the onset of heavy rainfall,  
650 providing valuable insights into the lead-up to extreme precipitation events. Infrasound and  
651 seismic data further complemented this analysis, with infrasound providing useful observations of

652 lightning activity and seismic data revealing the link between rainfall intensity and high-frequency  
653 seismic noise.

654 The storm analysed here represents an exceptional meteorological event and one of the most  
655 intense storms recorded in the region in recent years. According to the ClimaMeter analysis of  
656 Antonescu et al. (2024), the characteristics of this storm place it within the broader context of  
657 extreme events under changing climate conditions. The integration of GNSS, infrasound, and  
658 seismic data provides a more nuanced and holistic view of storm dynamics, highlighting the need  
659 for advanced monitoring systems to predict and respond to such extreme events. Looking forward,  
660 such multi-sensor approaches may support future developments in integrated environmental  
661 monitoring and research into early-warning capabilities, ultimately contributing to improved  
662 understanding and characterization of high-impact atmospheric events.

## 663 **7. Code availability**

664 Seismic data were processed with the open-source python framework for seismology Obspy  
665 (Beyreuther et al., 2010). Infrasound data was processed with the WinPMCC software (Le Pichon  
666 et al., 2010) developed by CEA/DASE (French Atomic Energy Commission, Environmental  
667 Assessment and Monitoring Department) and open-source Python libraries for signal processing.  
668 Some of the figures were made with GMT (Generic Mapping Tools, Wessel et al., 2019). The  
669 GNSS data was processed using Gamit/Globk (Herring et al., 2020) developed by Massachusetts  
670 Institute of Technology (<http://www-gpsg.mit.edu/gg/>).

## 671 **8. Data availability**

672 Processed infrasound, seismic, and GNSS-derived integrated water vapour data can be visualized  
673 and accessed via the INFP monitoring platforms: <https://infp.ro/dashboard-reactive.php> and  
674 <https://reactive.infp.ro/events/>. Seismic data are part of the Romanian National Seismic Network  
675 maintained by the National institute for Earth Physics (NIEP, [www.infp.ro](http://www.infp.ro)) and are freely  
676 available in the miniseed format via EIDA (European Integrated Data Archive,  
677 <https://www.orfeus-eu.org/data/eida/>). GNSS data are available for download from NIEP  
678 (<http://gps.infp.ro/#/download>) and are provided in the standardized RINEX v2 format, with 24-  
679 hour files sampled at 30-second intervals. Infrasound data at AGIR are available to download from  
680 NIEP via FDSN dataselect web service. Hourly hydro-meteorological data were obtained from the  
681 Copernicus Climate Change Service, Climate Data Store (<https://doi.org/10.24381/cds.bd0915c6>),  
682 ERA5 dataset (Hersbach et al., 2023). Limited wind and precipitation data were downloaded from  
683 the National Meteorological Agency from <https://www.meteoromania.ro/grafice/> (accessed on  
684 13.09.2024) and from [https://www.meteoromania.ro/clim/caracterizare-lunara/cc\\_2024\\_08.html](https://www.meteoromania.ro/clim/caracterizare-lunara/cc_2024_08.html)  
685 (accessed on 10.11.2025), respectively. Lightning data came from Meteosat Third Generation  
686 Lightning Imager operated by EUMETSAT (The European Organisation for the Exploitation of  
687 Meteorological Satellites, <https://www.eumetsat.int/>).

688

689

690

## 691 **9. Author contribution**

692 **Laura Petrescu:** Conceptualization, Methodology, Software, Formal analysis, Data Curation,  
693 Writing-Original Draft, Visualization; **Bogdan Antonescu:** Conceptualization, Writing-Review &  
694 Editing, Visualization; **Sorin Nistor:** Software, Formal Analysis, Data curation, Visualisation,  
695 Writing-Review & Editing; **Iustin Floroiu:** Methodology, Software, Formal analysis, Data  
696 Curation, Writing-Original Draft, Visualization; **Dragoş Ene:** Software, Formal analysis, Data  
697 Curation, Writing-Review & Editing; **Daniela Ghica:** Software, Formal analysis, Data Curation;  
698 **Constantin Ionescu:** Funding Acquisition, Resources, Project administration; **Andrei Anghel:**  
699 Methodology, Supervision; **Mihai Datcu:** Methodology, Supervision, Funding Acquisition,  
700 Resources, Project administration.

## 701 **10. Competing interests**

702 The authors declare that they have no conflict of interest.

## 703 **11. Acknowledgments**

704 We would like to thank the technicians and staff at NIEP for their support in installing,  
705 maintaining, and ensuring the proper functioning of the equipment used in this study. Additionally,  
706 we appreciate the efforts of those involved in data formatting and preparation (Cristian Neagoe,  
707 Eduard Nastase, Victorin Toader) which were essential for this work. We also thank the two  
708 anonymous reviewers for their valuable feedback, which helped improve the manuscript.

## 709 **12. Financial support**

710 This work was carried out in the framework of the “Competence Center for Climate Change Digital  
711 Twin for Earth forecasts and societal redressment” Project PNRR- DTEClimate nr.  
712 760008/31.12.2023, subproject Reactive “The Research center for climate change due to natural  
713 disasters and extreme weather events”, supported by the Ministry of Research, Innovation and  
714 Digitalization of Romania.

## 715 **13. References**

716 Antonescu, B., Dafis, S., & Faranda, D.: Changes in precipitation patterns driving August 2024  
717 Romania floods mostly driven by human-driven climate change. *ClimaMeter, Institut Pierre*  
718 *Simon Laplace, CNRS*. <https://doi.org/10.5281/zenodo.14056214>, 2024.

719 Ardhuin, F., Gualtieri, L., Stutzmann, E., Nakata, N. and Fichtner, A.: Physics of ambient noise  
720 generation by ocean waves. In *Seismic ambient noise*, Eds: Nakata, N., Gualtieri, L., Fichtner, A.  
721 Cambridge University Press, 69-108, <https://doi.org/10.1017/9781108264808.005>, 2019.

722 Assink, J. D., Evers, L. G., Holleman, I., and Paulssen, H.: Characterization of infrasound from  
723 lightning, *Geophysical Research Letters*, 35, L15802, <https://doi.org/10.1029/2008GL034193>,  
724 2008.

- 725 Aster, R.C., McNamara, D.E. & Bromirski, P.D.: Multidecadal climate-induced variability in  
726 microseisms. *Seismological Research Letters*, 79(2), 194-202,  
727 <https://doi.org/10.1785/gssrl.79.2.194>, 2008.
- 728 Aster, R.C., Ringler, A.T., Anthony, R.E., & Lee, T.A.: Increasing ocean wave energy observed  
729 in Earth's seismic wavefield since the late 20th century. *Nature Communications*, 14(1), 6984,  
730 <https://doi.org/10.1038/s41467-023-42673-w>, 2023.
- 731 Athanase, M., Sánchez-Benítez, A., Monfort, E., Jung, T. and Goessling, H.F.: How climate  
732 change intensified storm Boris' extreme rainfall, revealed by near-real-time storylines.  
733 *Communications Earth & Environment*, 5(1), 676, <https://doi.org/10.1038/s43247-024-01847-0>,  
734 2024.
- 735 Awange, J.L.: Environmental monitoring using GNSS: Global navigation satellite systems,  
736 Springer, Heidelberg, <https://doi.org/10.1007/978-3-540-88256-5>, 2012.
- 737 Beyreuther, M., Barsch, R., Krischer, L., Megies, T., Behr, Y. and Wassermann, J.: ObsPy: A  
738 Python toolbox for seismology. *Seismological Research Letters*, 81(3), 530-533,  
739 <https://doi.org/10.1785/gssrl.81.3.530>, 2010.
- 740 Bengtsson, L., Hodges, K.I. and Roeckner, E.: Storm tracks and climate change. *Journal of*  
741 *climate*, 19(15), 3518-3543, <https://doi.org/10.1175/JCLI3815.1>, 2006.
- 742 Bližňák, V. and Sokol, Z.: First validation of the Lightning Imager aboard Meteosat Third  
743 Generation satellite with Earth Networks Total Lightning Network. *International Journal of*  
744 *Applied Earth Observation and Geoinformation*, 147, 105205,  
745 <https://doi.org/10.1016/j.jag.2026.105205>, 2026.
- 746 Bollinger, L., Perrier, F., Avouac, J.P., Sapkota, S., Gautam, U., Tiwari, D.R.: Seasonal  
747 modulation of seismicity in the Himalaya of Nepal, *Geophysical Research Letters*, 34(8),  
748 <https://doi.org/10.1029/2006GL029192>, 2007.
- 749 Bondár, I., Šindelářová, T., Ghica, D., Mitterbauer, U., Liashchuk, A., Baše, J., Chum, J., Czanik,  
750 C., Ionescu, C., Neagoe, C. and Pásztor, M.: Central and Eastern European Infrasound Network:  
751 contribution to infrasound monitoring, *Geophysical Journal International*, 230(1), 565-579,  
752 <https://doi.org/10.1093/gji/ggac066>, 2022.
- 753 Borzì, A.M., Minio, V., Cannavò, F., Cavallaro, A., D'Amico, S., Gauci, A., De Plaen, R., Lecocq,  
754 T., Nardone, G., Orasi, A., Picone, M., Cannata, A.: Monitoring extreme meteo-marine events in  
755 the Mediterranean area using the microseism (Medicane Apollo case study). *Scientific Reports*,  
756 12(1), <https://doi.org/10.1038/s41598-022-25395-9>, 2022.

- 757 Bosy, J., Kaplon, J., Rohm, W., Sierny, J. and Hadas, T.: Near real-time estimation of water vapour  
758 in the troposphere using ground GNSS and the meteorological data, *Annales Geophysicae*, 30,  
759 1379–1391, <https://doi.org/10.5194/angeo-30-1379-2012>, 2012.
- 760 Brachet, N., Brown, D., Le Bras, R., Cansi, Y., Mialle, P., Coyne, J.: Monitoring the Earth's  
761 Atmosphere with the Global IMS Infrasound Network, in: *Infrasound Monitoring for Atmospheric*  
762 *Studies*, edited by: Le Pichon, A., Blanc, E., Hauchecorne, A. , Springer, Dordrecht,  
763 [https://doi.org/10.1007/978-1-4020-9508-5\\_3](https://doi.org/10.1007/978-1-4020-9508-5_3), 2010.
- 764 Bromirski, P.D. and Duennebieer, F.K.: The near-coastal microseism spectrum: Spatial and  
765 temporal wave climate relationships. *Journal of Geophysical Research: Solid Earth*, 107(B8), ESE  
766 5-1-ESE 5-20, <https://doi.org/10.1029/2001JB000265>, 2002.
- 767 Bruyninx, C., Habrich, H., Söhne, W., Kenyeres, A., Stangl, G. and Völksen, C.: Enhancement of  
768 the EUREF permanent network services and products, in: *Proceedings of the International*  
769 *Association of Geodesy, Symposium on Geodesy for Planet Earth, Buenos Aires, Argentina, 31*  
770 *August-4 September 2009*, 27-34, 2012.
- 771 Burtin, A., Hovius, N. and Turowski, J.M.: Seismic monitoring of torrential and fluvial processes.  
772 *Earth Surface Dynamics*, 4(2), 285-307, <https://doi.org/10.5194/esurf-4-285-2016>, 2016.
- 773 Butler, R. and Aucan, J.: Multisensor, microseismic observations of a hurricane transit near the  
774 ALOHA cabled observatory. *Journal of Geophysical Research: Solid Earth*, 123(4), 3027-3046,  
775 2018.
- 776 Campus, P. and Christie, D.R.: Worldwide observations of infrasonic waves, in: *Infrasound*  
777 *monitoring for atmospheric studies*, edited by: Le Pichon, A., Blanc, E., Hauchecorne, A.,  
778 Springer, Dordrecht, Netherlands, 185-234, [https://doi.org/10.1007/978-1-4020-9508-5\\_6](https://doi.org/10.1007/978-1-4020-9508-5_6), 2009.
- 779 Cansi, Y. and Pichon, A.L.: Infrasound event detection using the progressive multi-channel  
780 correlation algorithm, in: *Handbook of signal processing in acoustics.*, edited by: Havelock, D.,  
781 Kuwano, S., Vorländer, M., Springer, New York, 1425-1435, [https://doi.org/10.1007/978-0-387-](https://doi.org/10.1007/978-0-387-30441-0_77)  
782 [30441-0\\_77](https://doi.org/10.1007/978-0-387-30441-0_77), 2008.
- 783 Coates, A. and Ng, A.Y.: Learning feature representations with k-means. In *Neural Networks:*  
784 *Tricks of the Trade: Second Edition (561-580)*. Berlin, Heidelberg: Springer Berlin Heidelberg,  
785 2012.
- 786 Coviello, V., Palo, M., Adirosi, E. and Picozzi, M.: Seismic signature of an extreme hydro-  
787 meteorological event in Italy, *Natural Hazards*, 1(1), 17, [https://doi.org/10.1038/s44304-024-](https://doi.org/10.1038/s44304-024-00018-7)  
788 [00018-7](https://doi.org/10.1038/s44304-024-00018-7), 2024.
- 789 Diaz, J., Ruiz, M., Udina, M., Polls, F., Martí, D., Bech, J.: Monitoring storm evolution using a  
790 high-density seismic network, *Scientific Reports*, 13(1), [https://doi.org/10.1038/s41598-023-](https://doi.org/10.1038/s41598-023-28902-8)  
791 [28902-8](https://doi.org/10.1038/s41598-023-28902-8), 2023.

- 792 Díaz, J., Ruiz, M., Sánchez-Pastor, P.S. and Romero, P.: Urban seismology: On the origin of earth  
793 vibrations within a city. *Scientific reports*, 7(1), 15296, 2017.
- 794 Dimitriu, R.G., Stanciu, I.M., Barbu M.-B., Dobrev, N., Dumitru, P.: First results on the western  
795 Black Sea coast geodynamics resulted from GeoPontica permanent GNSS stations network data  
796 processing, in: Proceedings of the 17th International Multidisciplinary Scientific GeoConference  
797 SGEM, Albena, Bulgaria August 2017, 17(11), 149-157, 2017.
- 798 Dullaart, J.C., Muis, S., Bloemendaal, N. and Aerts, J.C.: Advancing global storm surge modelling  
799 using the new ERA5 climate reanalysis. *Climate Dynamics*, 54(1), 1007-1021, 2020.
- 800 Ebeling, C.W.: Inferring Ocean Storm Characteristics from Ambient Seismic Noise. A Historical  
801 Perspective, *Advances in Geophysics*, 53, 1-33. [https://doi.org/10.1016/B978-0-12-380938-](https://doi.org/10.1016/B978-0-12-380938-4.00001-X)  
802 [4.00001-X](https://doi.org/10.1016/B978-0-12-380938-4.00001-X), 2012.
- 803 Enno, S.-E., Viticchie, B., Navia, D. and Grandell, J.: Meteosat-12 Lightning Imager: first year of  
804 observations and the main performance characteristics, in: 12th European Conference on Severe  
805 Storms, 08 August 2025, <https://doi.org/10.5194/ecss2025-152>, 2025.
- 806 Faranda, D., Messori, G., Coppola, E., Alberti, T., Vrac, M., Pons, F., Yiou, P., Saint Lu, M., Hisi,  
807 A. N. S., Brockmann, P., Dafis, S., Mengaldo, G., and Vautard, R.: ClimaMeter: contextualizing  
808 extreme weather in a changing climate, *Weather Climate Dynamics*, 5, 959-983,  
809 <https://doi.org/10.5194/wcd-5-959-2024>, 2024.
- 810 Floroiu, I., Anghel, A., Petrescu, L. and Datcu, M.: Clustering and Feature-Based Similarity  
811 Retrieval of Infrasound Events during Two Storms in Constanța, Romania, *International*  
812 *Conference on Machine Intelligence for GeoAnalytics and Remote Sensing (MIGARS)*, Bucharest,  
813 Romania, 2025, 1-4, <https://doi.org/10.1109/MIGARS67156.2025.11231952>, 2025.
- 814 Francoeur, J.W., Matoza, R.S., Ortiz, H.D. and De Negri, R.: Identification of transient seismo-  
815 acoustic signals from crashing ocean waves: template matching and location of discrete surf  
816 events. *Geophysical Journal International*, 243(2), ggaf317, 2025.
- 817 Garcés, M.A.: On infrasound standards, part 1 time, frequency, and energy scaling. *InfraMatics*,  
818 2(2),13–35, <https://doi.org/10.4236/inframatics.2013.22002>, 2013.
- 819 Gastmeier, W.J. and Howe, B.: Recent studies of infrasound from industrial sources. *Canadian*  
820 *Acoustics*, 36(3), 58-59, 2008.
- 821 Grafkina, M.V., Nyunin, B.N. and Sviridova, E.Y: Environmental monitoring and simulation of  
822 infrasound generating mechanism of traffic flow. *Journal of Ecological Engineering*, 20(7),  
823 2019.
- 824 Grevemeyer, I., Herber, R. and Essen, H.H.: Microseismological evidence for a changing wave  
825 climate in the northeast Atlantic Ocean. *Nature*, 408(6810), 349-352,  
826 <https://doi.org/10.1038/35042558>, 2000.

- 827 Groos, J.C. and Ritter, J.R.R.: Time domain classification and quantification of seismic noise in  
828 an urban environment. *Geophysical Journal International*, 179(2), pp.1213-1231, 2009.
- 829 Gualtieri, L., Camargo, S.J., Pascale, S., Pons, F.M.E., & Ekström, G.: The persistent signature of  
830 tropical cyclones in ambient seismic noise, *Earth and Planetary Science Letters*, 484, 287-294.  
831 <https://doi.org/10.1016/j.epsl.2017.12.026>, 2018.
- 832 Guerova, G., Jones, J., Douša, J., Dick, G., de Haan, S., Pottiaux, E., Bock, O., Pacione, R.,  
833 Elgered, G., Vedel, H. and Bender, M.: Review of the state of the art and future prospects of the  
834 ground-based GNSS meteorology in Europe, *Atmospheric Measurement Techniques*, 9(11),  
835 5385–5406, <https://doi.org/10.5194/amt-9-5385-2016>, 2016.
- 836 Herring, T., King, R., Floyd, M., McClusky, S.: GAMIT Reference Manual GPS Analysis at MIT  
837 Release 10.7. GAMIT/GLOBK, 2020.
- 838 Hersbach, H., Bell, B., Berrisford, P., Hirahara, S., Horányi, A., Muñoz-Sabater, J., Nicolas, J.,  
839 Peubey, C., Radu, R., Schepers, D. and Simmons, A.: The ERA5 global reanalysis, *Quarterly*  
840 *Journal of the Royal Meteorological Society*, 146(730), 1999-2049, 2020.
- 841 Hersbach, H., Bell, B., Berrisford, P., Biavati, G., Horányi, A., Muñoz Sabater, J., Nicolas, J.,  
842 Peubey, C., Radu, R., Rozum, I., Schepers, D., Simmons, A., Soci, C., Dee, D., Thépaut, J.-N.:  
843 ERA5 hourly data on single levels from 1940 to present. Copernicus Climate Change Service  
844 (C3S) Climate Data Store (CDS), <https://doi.org/10.24381/cds.adbb2d47>, 2023.
- 845 Holmlund, K., Grandell, J., Schmetz, J., Stuhlmann, R., Bojkov, B., Munro, R., Lekouara, M.,  
846 Coppens, D., Viticchie, B., August, T. and Theodore, B.: Meteosat Third Generation (MTG):  
847 Continuation and innovation of observations from geostationary orbit, *Bulletin of the American*  
848 *Meteorological Society*, 102(5), E990-E1015, <https://doi.org/10.1175/BAMS-D-19-0304.1>, 2021.
- 849 Hua, J., Wu, M., Mulholland, J.P., Neelin, J.D., Tsai, V.C. and Trugman, D.T.: High-resolution  
850 precipitation monitoring with a dense seismic nodal array. *Scientific Reports*, 13(1), 11450,  
851 <https://doi.org/10.1038/s41598-023-38008-w>, 2023.
- 852 Hupe, P., Ceranna, L., Pilger, C., de Carlo, M., Le Pichon, A., Kaifler, B. and Rapp, M.: Assessing  
853 middle atmosphere weather models using infrasound detections from microbaroms. *Geophysical*  
854 *Journal International*, 216(3), 1761-1767, <https://doi.org/10.1093/gji/ggy520>, 2019.
- 855 Hupe, P., Ceranna, L., Le Pichon, A., Matoza, R.S. and Mialle, P.: International Monitoring  
856 System infrasound data products for atmospheric studies and civilian applications. *Earth System*  
857 *Science Data Discussions*, 14, 4201–4230, <https://doi.org/10.5194/essd-14-4201-2022>, 2022.
- 858 Iliescu, A. I., Rus, T., Danciu, V., Moldoveanu, C., & Ilie, A.: Current situation of GNSS networks  
859 in Romania, *Bulletin of University of Agricultural Sciences and Veterinary Medicine Cluj-Napoca.*  
860 *Horticulture*, 76(2), 2019.

- 861 Jakobsen, J.: Infrasound emission from wind turbines. *Journal of low frequency noise, vibration*  
862 *and active control*, 24(3), 145-155, 2005.
- 863 Jiao, D., Xu, N., Yang, F. and Xu, K.: Evaluation of spatial-temporal variation performance of  
864 ERA5 precipitation data in China. *Scientific Reports*, 11(1), 17956, 2021.
- 865 Johnston, G., Riddell, A. and Hausler, G.: The international GNSS service, in: Springer handbook  
866 of global navigation satellite systems, edited by: Teunissen, P.J. and Montenbruck, O., Springer,  
867 Cham, Switzerland, 967-982, [https://doi.org/10.1007/978-3-319-42928-1\\_33](https://doi.org/10.1007/978-3-319-42928-1_33), 2017.
- 868 Jones, J., Guerova, G., Douša, J., Dick, G., de Haan, S., Pottiaux, E., Bock, O., Pacione, R. and  
869 Van Malderen, R.: Advanced GNSS tropospheric products for monitoring severe weather events  
870 and climate, COST Action ES1206 Final Action Dissemination Report, 563, 2020.
- 871 Karabatić, A., Weber, R. and Haiden, T.: Near real-time estimation of tropospheric water vapour  
872 content from ground based GNSS data and its potential contribution to weather now-casting in  
873 Austria, *Advances in Space Research*, 47(10), 1691–1703,  
874 <https://doi.org/10.1016/j.asr.2010.10.028>, 2011.
- 875 Kober, K. and Tafferner, A.: Tracking and nowcasting of convective cells using remote sensing  
876 data from radar and satellite, *Meteorologische Zeitschrift*, 1(18), 75-84,  
877 <https://doi.org/10.1127/0941-2948/2009/359>, 2009.
- 878 Koper, K.D. & Burlacu, R.: The fine structure of double-frequency microseisms recorded by  
879 seismometers in North America. *Journal of Geophysical Research: Solid Earth*, 120(3), 1677-  
880 1691. <https://doi.org/10.1002/2014JB011820>, 2015.
- 881 Kokou, P.: Status of the MTG-I1 Lightning Imager commissioning activities, in: EUMETSAT  
882 Conference 2023, 1-C GEO – MTG, Malmö, Sweden, 12 September 2023, 2023.
- 883 Landès, M., Ceranna, L., Le Pichon, A. and Matoza, R.S.: Localization of microbarom sources  
884 using the IMS infrasound network. *Journal of Geophysical Research: Atmospheres*, 117(D6),  
885 <https://doi.org/10.1029/2011JD016684>, 2012.
- 886 Landskron, D., Böhm, J.: VMF3/GPT3: refined discrete and empirical troposphere mapping  
887 functions, *Journal of Geodesy*, 92, 349–360, <https://doi.org/10.1007/s00190-017-1066-2>, 2018.
- 888 Li, L., Boué, P., Retailleau, L., & Campillo, M.: Spatiotemporal Correlation Analysis of Noise-  
889 Derived Seismic Body Waves With Ocean Wave Climate and Microseism Sources, *Geochemistry,*  
890 *Geophysics, Geosystems*, 21(9), <https://doi.org/10.1029/2020GC009112>, 2020.
- 891 Listowski, C., Forestier, E., Dafis, S., Farges, T., De Carlo, M., Grimaldi, F., Le Pichon, A.,  
892 Vergoz, J., Heinrich, P. and Claud, C.: Remote monitoring of Mediterranean hurricanes using  
893 infrasound, *Remote Sensing*, 14(23), 6162, <https://doi.org/10.3390/rs14236162>, 2022.

894 MacQueen, J.: Some methods for classification and analysis of multivariate observations, in:  
895 Proceedings of the Fifth Berkeley Symposium on Mathematical Statistics and Probability,  
896 Berkeley, California, January 1967, 5, 281-298, 1967.

897 Marut, G., Hadas, T., Kaplon, J., Trzcina, E. and Rohm, W.: Monitoring the water vapor content  
898 at high spatio-temporal resolution using a network of low-cost multi-GNSS receivers, *IEEE*  
899 *Transactions on Geoscience and Remote Sensing*, 60, 1-14,  
900 <https://doi.org/10.1109/TGRS.2022.3226631>, 2022.

901 Nistor, S., Suba, N.S., Maciuk, K., Kudryś, J., Nastase, E.I. and Muntean, A.: Analysis of noise  
902 and velocity in GNSS EPN-repro 2 time series, *Remote Sensing*, 13(14), 2783,  
903 <https://doi.org/10.3390/rs13142783>, 2021a.

904 Nistor, S., Suba, N.S., El-Mowafy, A., Apollo, M., Malkin, Z., Nastase, E.I., Kudryś, J. and  
905 Maciuk, K.: Implication between geophysical events and the variation of seasonal signal  
906 determined in GNSS position time series, *Remote Sensing*, 13(17), 3478,  
907 <https://doi.org/10.3390/rs13173478>, 2021b.

908 Pásztor, M., Czanik, C. and Bondár, I.: A single array approach for infrasound signal  
909 discrimination from quarry blasts via machine learning, *Remote Sensing*, 15(6), 1657,  
910 <https://doi.org/10.3390/rs15061657>, 2023.

911 Le Pichon, A., Matoza, R., Brachet, N. and Cansi, Y.: Recent enhancements of the PMCC  
912 infrasound signal detector. *Inframatics*, 26, 5-8, 2010.

913 Price, I., Sanchez-Gonzalez, A., Alet, F., Andersson, T.R., El-Kadi, A., Masters, D., Ewalds, T.,  
914 Stott, J., Mohamed, S., Battaglia, P. and Lam, R.: Probabilistic weather forecasting with machine  
915 learning. *Nature*, 637(8044), 84-90, 2025

916 Priego, E., Jones, J., Porres, M.J. and Seco, A.: Monitoring water vapour with GNSS during a  
917 heavy rainfall event in the Spanish Mediterranean area, *Geomatics, Natural Hazards and Risk*,  
918 8(2), 282–294, <https://doi.org/10.1080/19475705.2016.1201150>, 2017.

919 Retailleau, L. & Gualtieri, L.: Multi-phase seismic source imprint of tropical cyclones, *Nature*  
920 *Communications*, 12(1), <https://doi.org/10.1038/s41467-021-22231-y>, 2021.

921 Rindraharisaona, E.J., Réchou, A., Fontaine, F.R., Barruol, G., Stamenoff, P., Boudevillain, B.,  
922 Rigaud-Louise, F. and Delcher, E.: Seismic signature of rain and wind inferred from seismic data,  
923 *Earth and Space Science*, 9(10), p.e2022EA002328, 2022.

924 Šindelářová, J., Chum, J., Skripnikova, K., and Base, J.: Atmospheric infrasound observed during  
925 intense convective storms on 9–10 July 2011, *Journal of Atmospheric and Solar-Terrestrial*  
926 *Physics*, 122, 66–74, <https://doi.org/10.1016/j.jastp.2014.10.014>, 2015.

- 927 Šindelářová, T., De Carlo, M., Czanik, C., Ghica, D., Kozubek, M., Podolská, K., Baše, J., Chum,  
928 J., and Mitterbauer, U.: Infrasound signature of the post-tropical storm Ophelia at the Central and  
929 Eastern European Infrasound Network, *Journal of Atmospheric and Solar-Terrestrial Physics*, 217,  
930 105603, <https://doi.org/10.1016/j.jastp.2021.105603>, 2021.
- 931 Smirnov, A., De Carlo, M., Le Pichon, A., Shapiro, N.M. and Kulichkov, S.: Characterizing the  
932 oceanic ambient noise as recorded by the dense seismo-acoustic Kazakh network. *Solid Earth*,  
933 12(2), 503-520, 2021.
- 934 Soci, C., Hersbach, H., Simmons, A., Poli, P., Bell, B., Berrisford, P., Horányi, A., Muñoz-Sabater,  
935 J., Nicolas, J., Radu, R. and Schepers: The ERA5 global reanalysis from 1940 to 2022. *Quarterly*  
936 *Journal of the Royal Meteorological Society*, 150(764), 4014-4048, 2024.
- 937 Sokol, Z., Szturc, J., Orellana-Alvear, J., Popova, J., Jurczyk, A. and Célleri, R.: The role of  
938 weather radar in rainfall estimation and its application in meteorological and hydrological  
939 modelling—A review, *Remote Sensing*, 13(3), 351, 2021.
- 940 Stopa, J.E., Cheung, K.F., Garcés, M.A. and Badger, N.: Atmospheric infrasound from nonlinear  
941 wave interactions during Hurricanes Felicia and Neki of 2009, *Journal of Geophysical Research:*  
942 *Oceans*, 117(C12), <https://doi.org/10.1029/2012JC008257>, 2012
- 943 Stott, P.: How climate change affects extreme weather events. *Science*, 352(6293), 1517-1518,  
944 <https://doi.org/10.1126/science.aaf7271>, 2016.
- 945 Tanimoto, T. & Anderson, A.: Seismic noise between 0.003 Hz and 1.0 Hz and its classification,  
946 *Progress in Earth and Planetary Science*, 10(1), <https://doi.org/10.1186/s40645-023-00587-7>,  
947 2023.
- 948 Taweesintananon, K., Landrø, M., Potter, J.R., Johansen, S.E., Rørstadbotnen, R.A., Bouffaut, L.,  
949 Kriesell, H.J., Brenne, J.K., Haukanes, A., Schjelderup, O. and Storvik, F.: Distributed acoustic  
950 sensing of ocean-bottom seismo-acoustics and distant storms: A case study from Svalbard,  
951 Norway. *Geophysics*, 88(3), B135-B150, 2023.
- 952 Tiberia, A., Mascitelli, A., D'adderio, L.P., Federico, S., Marisaldi, M., Porcù, F., Realini, E.,  
953 Gatti, A., Ursi, A., Fuschino, F. and Tavani, M.: Time evolution of storms producing terrestrial  
954 gamma-ray flashes using ERA5 reanalysis data, GPS, lightning and geostationary satellite  
955 observations. *Remote Sensing*, 13(4), 784, 2021.
- 956 Vaquero-Martínez, J. and Antón, M.: Review on the role of GNSS meteorology in monitoring  
957 water vapor for atmospheric physics, *Remote Sensing*, 13(12), 2287,  
958 <https://doi.org/10.3390/rs13122287>, 2021.
- 959 Viticchie, B., Lekouara, M., Hungershofer, K., Joro, S., Grandell, J., Maufrais, A., Marquez, M.J.,  
960 Munro, R.: Algorithm Theoretical Basis Document (ATBD) for L2 processing of the MTG  
961 Lightning Imager data, Rapp. Tech. EUMESTAT, 6, 2020.

- 962 Waxler, R., Frazier, W. G., Talmadge, C. L., Liang, B., Hetzer, C., Buchanan, H., and Audette, W.  
963 E.: Analysis of infrasound array data from tornadic storms in the southeastern United States,  
964 *Journal of the Acoustical Society of America*, 156, 1903–1919,  
965 <https://doi.org/10.1121/10.0028815>, 2024.
- 966 Wessel, P., Luis, J.F., Uieda, L.A., Scharroo, R., Wobbe, F., Smith, W.H. and Tian, D.: The generic  
967 mapping tools version 6, *Geochemistry, Geophysics, Geosystems*, 20(11), 5556-5564,  
968 <https://doi.org/10.1029/2019GC008515>, 2019.
- 969 Wilgan, K., Rohm, W. and Bosy, J.: Multi-observation meteorological and GNSS data comparison  
970 with numerical weather prediction model, *Atmospheric Research*, 156, 29–42,  
971 <https://doi.org/10.1016/j.atmosres.2014.12.011>, 2015.
- 972 Wu, G., Qin, S., Mao, Y., Ma, Z. and Shi, C.: Validation of precipitation events in ERA5 to gauge  
973 observations during warm seasons over eastern China. *Journal of Hydrometeorology*, 23(5), 807-  
974 822, 2022.  
975